



# Time-resolved particle image velocimetry measurements of a tandem jet array in a crossflow at low velocity ratios

Paul J. Kristo<sup>1</sup> · Mark L. Kimber<sup>2</sup> 

Received: 3 September 2020 / Revised: 18 December 2020 / Accepted: 1 February 2021 / Published online: 15 March 2021  
© The Author(s), under exclusive licence to Springer-Verlag GmbH, DE part of Springer Nature 2021

## Abstract

Investigation of the near field dynamics of a single and tandem array of three jets are provided by 2-D time-resolved particle image velocimetry (TR-PIV) measurements. Instantaneous velocity fields are examined in the transverse and spanwise planes with jet to crossflow velocity ratios in the range from 0.9 to 1.7. Previous studies have shown that for high ratios ( $\geq 2$ ), the leading jet provides sufficient shielding to ensure that all jets downstream exhibit nearly identical flow characteristics. The current transverse plane measurements exhibit more unique and localized features as a result of the competing effects of pressure gradients and vortex mechanisms assessed via the jet exit profiles, first and second order turbulent statistics, streamline trajectories, recirculation areas and penetrations depths. Proper orthogonal decomposition (POD) is applied to the spanwise plane instantaneous velocity fields to determine the statistically dominant features of the single and tandem jet configurations at equivalent velocity ratios. The velocity fields are then reconstructed using the truncated POD modes to provide further insight into the shear layer and wake vortices that drive these configurations. Vortex identification algorithms are applied to the reconstructed velocity fields to determine the statistical characteristics of the vortices, including their centroids, populations, areas and strengths, each of which exhibit largely different dependencies on jet configuration and velocity ratio. Several of the investigated metrics are found to exhibit different behaviors below and above a velocity ratio of unity and also as a function of increasing velocity ratio between 1 and 2, implying that several transitions mechanisms are present in the low velocity ratio regime investigated herein.

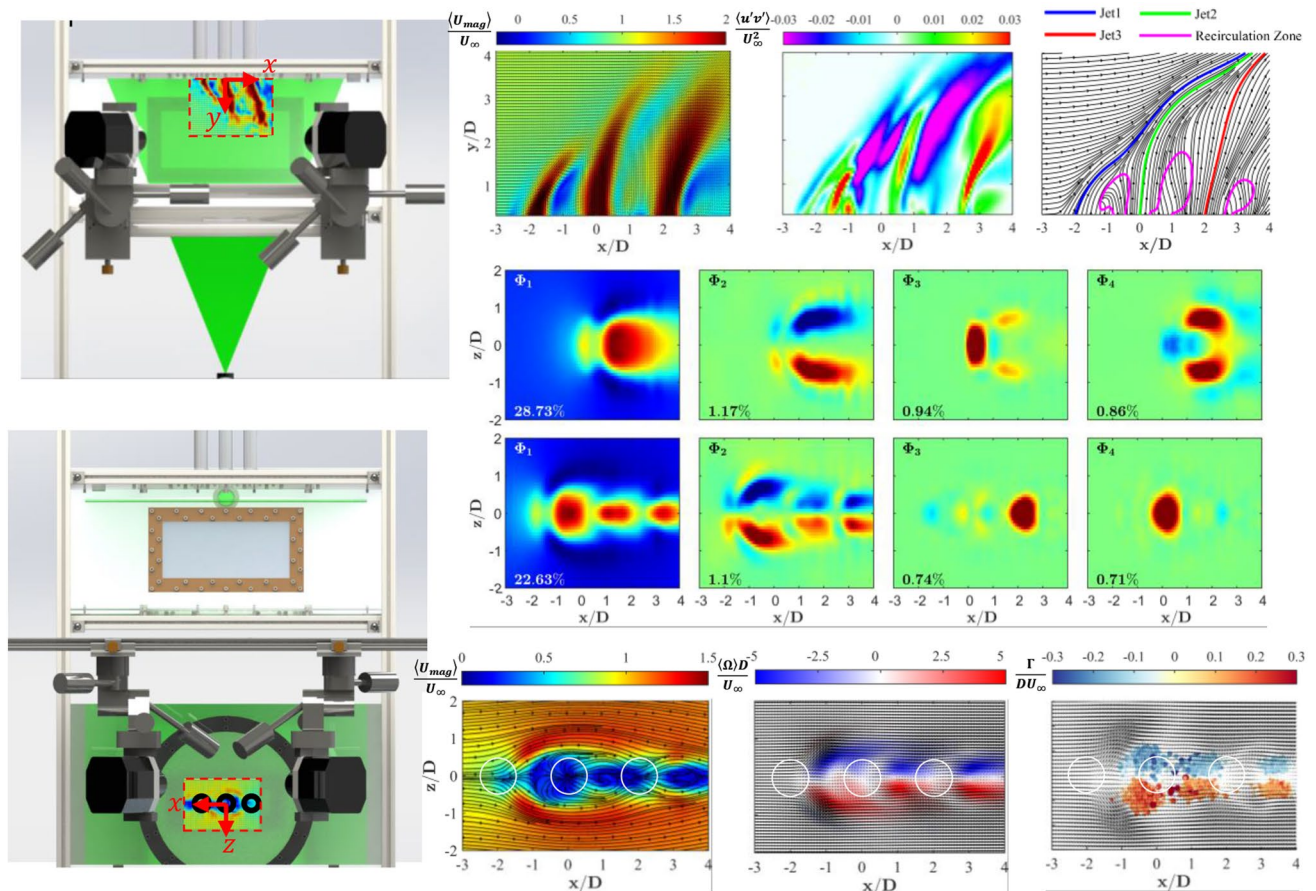
---

✉ Mark L. Kimber  
mark.kimber@tamu.edu

<sup>1</sup> Department of Mechanical Engineering, Texas A&M University, AIEN M104, 423 Spence Street, College Station, Texas 77843, USA

<sup>2</sup> Department of Nuclear Engineering, Department of Mechanical Engineering, Texas A&M University, AIEN 205D, 423 Spence Street, College Station, Texas 77843, USA

## Graphic abstract



## 1 Introduction

The jet in crossflow, or transverse jet, is found in a variety of industrial operations and natural occurrences, promoting a wealth of research efforts into its measurement, simulation and control. Interest stems from the flow's rich mixing and dispersion characteristics; affecting both the kinematic and scalar properties of applications including air breathing propulsion systems (Karagozian 2010), power generation (Amini et al. 2009), turbomachinery (Bons et al. 2002) and even volcanic plumes and wind currents (Gardner et al. 2007), among many others. From the design perspective, ongoing interests involve jet placement (flush with or protruding from wall), angled injection, alternate orifice shapes and the inclusion of additional jets and how these design features influence hydraulic, thermal and chemical mixing across all flow regimes. These parameters represent passive control features of the jet in crossflow which are well received throughout the literature. More recent active control

research topics largely center around the design of open loop jet controllers to optimize the vortex structures of the jet in crossflow (M'Closkey et al. 2002). Flow control allows for the jet in crossflow to act as an actuator for the anticipated acoustics (Shapiro et al. 2006), entrainment (Narayanan et al. 2003), drag reduction (Crafton et al. 2015; Lohse et al. 2016), or combustion (Anazadehsayed et al. 2017) response of the engineered system. Indeed, a wide variety of motivations exist for the jet in crossflow, however the current study is focused on incompressible, low jet to crossflow velocity ratios ( $< 2$ ) in multiple tandem arrays. It is useful then to compare the influence of repetitive tandem arrays to their unit flow basis.

The single round jet in crossflow is known to exhibit a rich set of physical responses most commonly depicted by the jet to crossflow velocity ratio ( $V_j/U_\infty$ ) or momentum flux ratio ( $\rho_j V_j^2 / \rho_\infty U_\infty^2$ ). These are broadly defined as "low" and "high" ratios in which the crossflow or jet dominates, respectively and are further complicated by the exit velocity profile

shape. These shapes are strongly a result of the jet configuration, where top hat or parabolic profiles are induced by nozzles and round pipes, respectively (Muppidi et al. 2005; New et al. 2006), both found frequently in application. Several authors have conducted experimental and numerical investigations to reveal four major vortical structures from the canonical arrangement including (a) horseshoe vortices, (b) jet shear layer vortices, (c) wake vortices and (d) counter-rotating vortex pairs (Mahesh 2013) each of which are found to vary in significance as a function of the characteristic ratio.

Planar laser-induced fluorescence (PLIF) measurements by Smith et al. (1998) have confirmed that the development of the counter rotating vortex pair formation is inversely proportional to the velocity ratio. Kelso et al. (1996) utilized hot-wire anemometry measurements in the range  $2 \leq V_j/U_\infty \leq 6$  to conclude that the jet flow and windward side boundary layer interaction produce steady horseshoe vortices at low velocity ratios and develop Kelvin–Helmholtz shear layer rollup and shedding as the velocity ratio increases. Likewise, for low velocity ratios, Gopalan et al. (2004) have confirmed the presence of a semi-cylindrical layer of wake vortices behind the jet, forming a small flow reversal. Meyer et al. (2007) provided the first use of Proper Orthogonal Decomposition (POD) on the jet in crossflow. Their work confirmed that the shear layer vortices are dominant in comparison to the wake vortices at low velocity ratios and that these features are decoupled from each other. An excellent investigation into the transition process from low to high velocity ratios was conducted by Cambonie et al. (2014), whose volumetric particle image velocimetry (PIV) measurements, confirmed that the classical jet in crossflow topology is not recovered until  $V_j/U_\infty > 1.25$ . Below this value, the authors describe a “progressive disappearance” of the leading edge vortices and strengthened interaction with the boundary layer. Each of these vortex phenomena strongly contribute to the velocity, temperature and concentration maxima, boundary and shear layer stability, jet spread and the size and proximity of the reverse flow region.

Several authors have proposed scaling laws and associated length scales that pertain to specific ranges of velocity or momentum ratios, with an extensive review provided by Margason (1993). Even after decades of investigation however, there is no one universally accepted scaling law for the jet in crossflow as a result of these transition processes, though the current authors recognize the efforts of Cambonie et al. (2013) to expand the scaling laws to incorporate boundary layers effects and consider it a significant improvement. However, in keeping with the current motivation, these effects are only further complicated with the introduction of multiple jets.

Studies involving multiple transverse jets consist of a variety of one and two dimensional arrays in inline, tandem,

or staggered orientations. Inline and staggered arrays have been historically motivated by applications in heat transfer and combustion (Florschuetz et al. 1987; Florschuetz et al. 1981; Huang et al. 1998; Ziegler et al. 1973). The current motive focuses on the tandem orientation. Several researchers have observed that the leading jet exhibits similar features to a single jet and that this leading jet provides a shielding effect on its downstream neighbor(s). This inhibits the influence of the crossflow on these secondary jets, thereby allowing them to penetrate further into the freestream (Gutmark et al. 2011; New et al. 2015; Ziegler et al. 1973). New et al. (2015) have confirmed that the shielding effects are strongly a function of their twin jet’s spacing and state that with sufficient downstream distance, the jets merge to form a single trajectory. Utilizing a similar twin tandem geometry, Gutmark et al. (2011) have compared the near field jet trajectories, penetrations and reverse flow regions produced by both jets, noting the deeper penetrations and larger reverse flow regions in comparison to their single jet. The works of Kolář et al. (2003, 2007) have described the mechanisms by which these differences occur, pointing to the large-scale vortical structures as the predominant feature. In particular, they conclude that the secondary counter rotating vortex pair dominates the mean flow behavior reducing shearing along the centerline of the pair, inducing recirculation downstream.

Multiple tandem jet studies typically employ a twin configuration, providing the most fundamental exchange. Experimental studies exceeding two jets are less common in the literature, though an excellent experiment is provided by Yu et al. (2006) and their PIV/PLIF measurements of a four jet array. They determined that for velocity ratios in the range of 2 to 8, the shielding and entrainment incurred by the leading jet promote nearly identical jet trajectories for all jets downstream. This is in contrast to the numerical results of Li et al. (2012), who studied 2, 3 and 4 tandem jet arrays with the Reynolds Averaged Navier–Stokes (RANS) realizable  $k-\epsilon$  model. Their results suggest that the last jet penetrates deeper as the number of jets increases and note that the shielding of the front jet declines with increasing jet spacing. More recent numerical efforts by Ling et al. (2016) highlight the shortcomings of typically employed RANS model assumptions compared to Large Eddy Simulation (LES) data (Ruiz et al. 2015) in effectively capturing the jet in crossflow physics. The authors employed random forest regressors to successfully tune the model for improved prediction of the Reynolds stress anisotropy, signifying a promising step forward. Several challenges exist then, for determining physical expressions and scaling for multiple jets in a crossflow and are here summarized in three major categories: (1) an ever-expanding list of geometric and kinematic variables that encompass the motivated physics and scaling, (2) experimental facilities capable of providing nominal modeling conditions for multiple jets in a

crossflow and (3) resolution/accuracy limitations/costs for three dimensional measurement techniques and simulations alike. Towards this end, the objectives of this investigation are as follows:

1. Introduce an experimental facility with independent control of three jets promoting high fidelity measurements at low jet to crossflow velocity ratios ( $< 2$ ).
2. Characterize the spatio-temporal nature of the single and tandem jet in crossflow in the transverse plane, identifying similar/contrasting behaviors as a result of competing pressure gradients and vortex formations.
3. Leverage the time resolved spanwise plane measurements with POD and vortex identification algorithms to provide new insights into the vortex statistics present in the wake of the single and tandem jets.
4. Provide sufficient supplemental data to serve future computational modeling efforts that seek to capture the interactions of tandem jets in a crossflow at low velocity ratios.

## 2 Methodology

A low-speed, closed loop wind tunnel supplies the freestream velocity or crossflow for the current investigation. The tunnel has undergone extensive preliminary diagnostics (Kristo et al. 2020) which verify a fully developed top hat inlet profile to the test section. A secondary flow motivation system consisting of a dedicated blower and PLC control system (Landfried et al. 2019) is utilized for independent flow control of each of the three jets. Experimental measurements are performed using a time-resolved particle image velocimetry (TR-PIV) system and several reference probes.

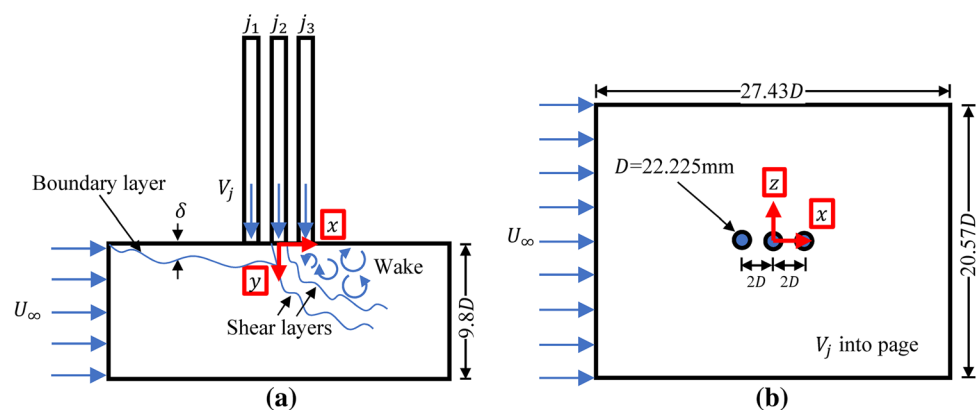
### 2.1 Experimental setup

The experimental test section is displayed in Fig. 1 and consists of three distinct tandem jets issuing vertically

downward from the ceiling. The three jet tandem array consists of the upstream leading jet 1, the middle jet 2 and the furthest downstream jet 3. The corresponding single jet experiments incorporate the middle (jet 2) pipe, while the upstream and downstream jets are off and carefully sealed flush on the ceiling. The axial centerline exit location of jet 2 (and corresponding single jet) constitutes the origin of the coordinate system, where  $x$  is the streamwise or cross flow direction,  $y$  is the transverse or jet direction and  $z$  is the spanwise direction, or ‘spread’ of the jet(s) in crossflow. The tunnel test section measures  $609.6 \times 217.7 \times 457.2$  mm in the  $x$ ,  $y$  and  $z$  directions respectively. Each of the jets is comprised of two identical aluminum tubes joined by a custom coupling. At the center of the coupling is a honeycomb flow straightener with wall thickness 0.53 mm, flat-to-flat hex cell of length 2.17 mm and is 76.20 mm in length. The internal diameter of a given jet is  $D=22.225$  mm and the triple jet configuration incorporates a  $2D$  center-to-center spacing along the streamwise direction.

Preliminary and supplemental measurements ensure properly specified experimental testing conditions and further delineation of the observed thermal fluid physics. Preliminary PIV tunnel inlet measurements (Kristo, Sohail, Reed and Kimber 2020) verify a fully-developed top hat inlet profile with spatially-averaged freestream velocity,  $U_\infty = 9.52$  m/s, corresponding Reynolds number,  $Re_\infty = 1.82 \times 10^5$  and turbulent kinetic energy,  $k = 0.57$  m<sup>2</sup>/s<sup>2</sup>, held constant for all proposed test cases. In lieu of boundary layer measurements, we employ the analytical solution for boundary layer thickness for a flat plate as informed by  $Re_\infty$  and the approximation of a 1/7-power law velocity profile (Pritchard 2011). Theoretical boundary layer thickness estimates are calculated at the axial centerline  $x$ -coordinate of each jet as  $\delta = 8.83$  mm, 10.33 mm and 11.84 mm for the first, second and third tandem jet, respectively. Preliminary PIV jet exit calibrations were also performed, with the tunnel system off, as originally part of a separate jet impingement investigation (Reed et al. 2020). The calibrations included six repeatable trials, across the entire operating spectrum of the

**Fig. 1** Schematic of the experimental test section and key flow features as seen from the **(a)**  $xy$  and **(b)**  $xz$  planes. Note that **(a)** incorporates the flow features of the single jet only and that each jet in tandem array exhibits these same redundant features with secondary interactions





secondary flow motivation system to ensure high accuracy in the appointed flow rates. The uni-directional velocity profile of each jet is spatially-averaged to yield the jet exit velocities,  $V_j$  and corresponding mass flow rates. The jets are spaced sufficiently far apart to ensure that the exit profiles do not exhibit entrainment. Each of the three jets in the tandem jet formation, as well as the single jet, are found to exhibit linear relationships, as expected, between user controlled flow rate and jet exit velocities. These extensive preliminary calibrations also ensure that the expected single and tandem jet velocity ratios are nearly identical for each of the three proposed test cases. This allows for comparison between the single and tandem jet configurations at a given jet to crossflow velocity ratio. Three jet to crossflow velocity ratio cases are proposed for the single and triple jet configurations with all relevant thermal fluid parameters fully delineated

in Appendix (Tables 3 and 4). The velocity ratios for each geometry are found to deviate within a maximum of 2.4% of one another, considered a good basis for comparison. For convenience, the remainder of this study approximates the three velocity ratio test cases as  $V_j/U_\infty = 0.9, 1.25, 1.7$ .

The experimental investigation consists of two principle measurement planes and corresponding optical arrangements as displayed in Fig. 2a, c and d for the  $xy$  and  $xz$  results, respectively. Measurements in the  $xy$  plane are conducted along the centerline ( $z=0$ ) of the jets and test section, providing indication of each jet's penetration into the crossflow. Observations from the  $xy$  plane measurements helped to inform a suitable location for the  $xz$  measurements, from which the jet spreading and wake formations can be observed further. As such, the  $xz$  measurements are conducted at  $y/D=1$ . Details regarding the TR-PIV hardware

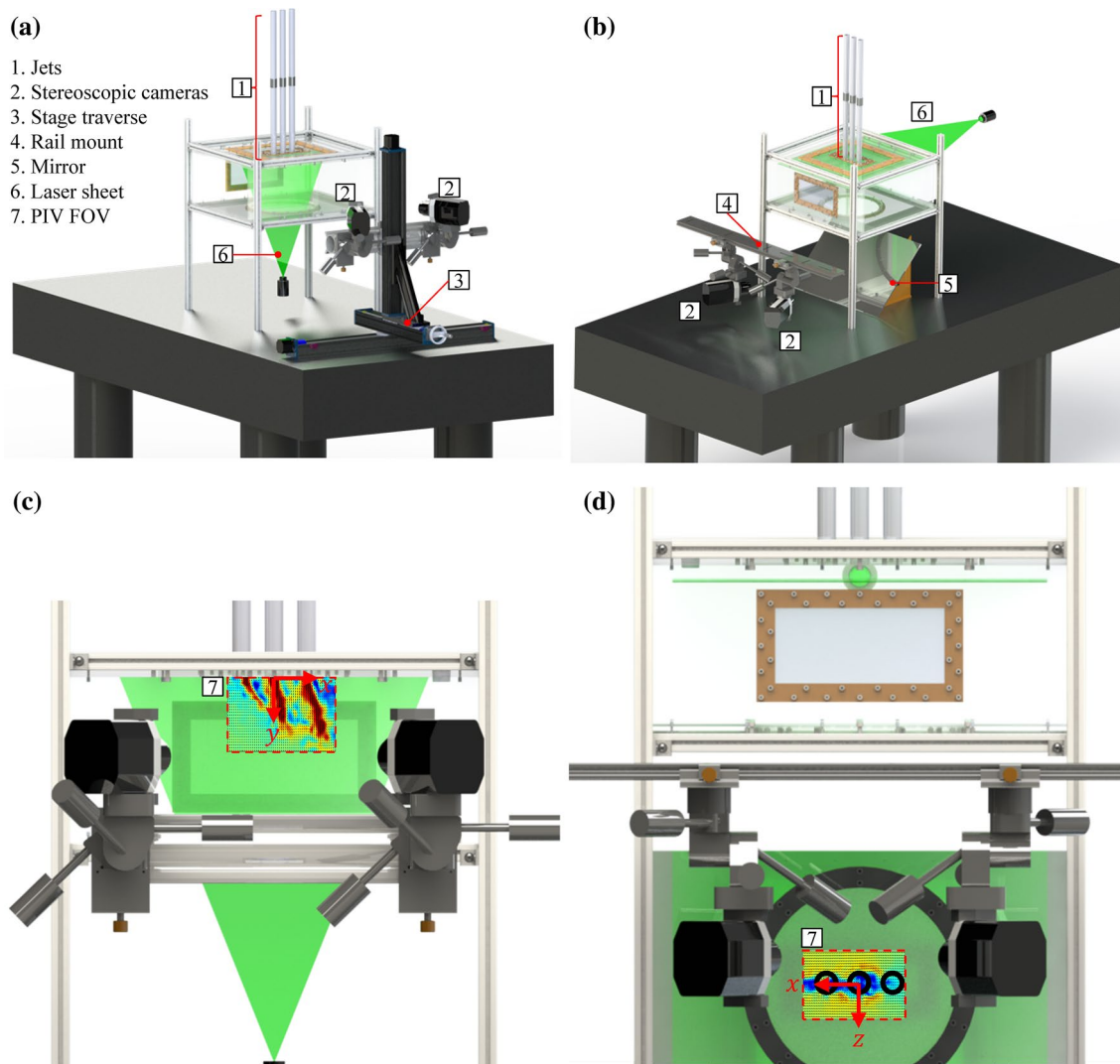


**Fig. 2** Experimental test section and equipment configurations for tandem jet study including **a**  $xy$  plane measurements, **b**  $xz$  plane measurements **c** close up of  $xy$  TR-PIV field of view (FOV), **d** close up of  $xz$  FOV

specifications are deferred to the next section, while their configurations are described here. As detailed in Fig. 2a, a Velmex Bi-Slide three-axis linear stage is incorporated for  $xy$  measurements, consisting of a straight line accuracy of  $\pm 0.076$  mm and rigidly mounted to the Newport RS2000-48–12 optical table. For the  $xz$  measurements, tight space constraints necessitated the use of a high-quality silvered mirror underneath the test section, pictured in Fig. 2b, d. The mirror is constrained at a  $45^\circ$  angle by two speed squares also rigidly mounted to the table. A Linos FLS 95 Rail substitutes the linear stages in this configuration with suitable framing (not pictured).

## 2.2 Time-resolved particle image velocimetry

In both measurement configurations, a stereoscopic camera configuration is utilized in conjunction with a laser sheet to provide high accuracy two dimensional – two component (2D–2C) TR-PIV. The high speed cameras are each Phantom Miro M120's with a 12 bit dynamic range and maximum resolution of  $1920 \times 1200$  pixels. Each camera utilizes a LaVision Scheimpflug Mount to alleviate perspective distortion from the stereoscopic configuration. A Nikon AF NIKKOR 50 mm f/1.8D lens and a LaVision Inc. 527 nm lens filter with 10 nm band pass and 70% transmission efficiency complete each camera's assembly. The laser sheet is generated by a Photonics Industries DM30-527-DH laser with a maximum power of 60 mJ/pulse at 527 nm and a laser sheet thickness of approximately 1.0 mm. A LaVision Laser Guiding Arm connects the laser to its focusing lens. For the  $xy$  measurements, the focusing lens (and corresponding laser sheet) is precisely placed using a Newport 433 Series translation stage with an angular deviation of  $< 200$  rad $\mu$ . The  $xz$  measurements incorporated the aforementioned Velmex Bi-Slide three axis linear stages. The laser sheet is precisely aligned using a digital level and calipers for each configuration. After precise alignment, the cameras and laser plane are calibrated using a LaVision 106–10 calibration target. A pinhole fit is selected and a scale factor of 5.41209 and 4.59372 px/mm are determined for the  $xy$  and  $xz$  planes, respectively. For testing, Dioctyl Sebacate seeder particles are generated by a TSI atomizer with only two of the seeder jets utilized. The crossflow is first seeded just upstream of the tunnel fan for 30 s, followed by 7 s of additional seeding for each test case through the secondary flow motivation for the jets. This provided an optimal seeding density between the tunnel and jets for the current investigation. For both planes, 2600 frames are captured at 1 kHz using a  $960 \times 824$  px field of view.

TR-PIV images are processed using LaVision DaVis 8.4.0 software. Image pre-processing utilizes a Butterworth high pass filter with a filter length of 7 images to limit background noise. Vector processing is accomplished

by the stereo-cross correlation algorithm with two initial passes using a  $64 \times 64$  pixel window with 1:1 square weighting and 75% overlap. Four final passes complete the vector generation, using a  $32 \times 32$  pixel window with an adaptive PIV grid with 75% overlap. The adaptive PIV grid adjusts the interrogation window and size to optimize local seeding density and flow gradients. This provides a robust method for improved accuracy in the instantaneous flow fields, at the expense of additional processing time. The stereoscopic configuration enables image correction and high accuracy mode is prompted for the final passes. The first post-processing step applies a 'strongly remove & iteratively replace' median filter, which removes vectors if the difference to the average is greater than  $2 \times$  root mean square (RMS) of its neighbors and re-inserts the vector if the difference to the average is less than  $3 \times$  RMS of its neighbors. At this stage, the true measurement data is not compromised and the statistical properties of the flow and their uncertainties are determined. There may exist however, small holes in the velocity fields, where vectors are not re-inserted, which is less than ideal for temporal analysis or mathematical operators (gradient, divergence, curl, etc.). As such, a final post-processing step is utilized: a vector interpolation fills any missing data by taking the average of all non-zero neighboring vectors, with a minimum of two such vectors required. In total, six repeatable trials are conducted for the  $xy$  plane and just one trial for the  $xz$  plane. The repeatable trials provide the random uncertainty contribution,  $s_i$ , calculated at each vector location using the student's t-distribution with 5 degrees of freedom and 95% confidence, i.e.  $s_i = t_{v=5, P=95\%} \sigma_x^-$  where here only,  $\sigma_x^-$  is the standard deviation of the means of an arbitrary metric. The systematic uncertainty,  $b_i$ , is calculated for the ensembled averaged velocity fields only according to the correlation statistics method of Wieneke (2015). This method leverages the intensity patterns of subsequent images to derive a relationship between the standard deviation of the intensity differences in each window and the expected asymmetry of the correlation peak and thereby the uncertainty of a displacement vector. The random and systematic uncertainty contributors are combined via a root mean sum of the squares to form the total uncertainty,  $u_i$  in the corresponding mean velocities. Standard convention for the systematic uncertainty of propagated statistics (i.e. RMS velocity, Reynolds stresses, etc.) is still an ongoing research topic in PIV measurement science (Sciacchitano et al. 2016; Smith et al. 2018). Propagated uncertainties in the current work are therefore explicitly based on the random uncertainty contribution only.

## 2.3 Reference probes

Non-obtrusive reference measurements are conducted in-situ alongside the TR-PIV measurements. These include

ambient temperature, pressure and humidity readings. Ambient humidity measurements are provided by an Omega HX93BDV1 relative humidity transmitter. An Apogee Instruments Model SB-100 barometric pressure transducer supplies the ambient pressure readings. All temperature measurements are provided by type T thermocouples with a crushed ice bath reference point. The relative humidity and ambient pressure sensors incorporate manufacturer curve fits. The thermocouples have undergone twelve repeatable calibrations using an automated Isotech Calisto 2250S Dry Block Calibrator, Model 935–14–61 platinum resistance thermometer reference probe and MilliK data logger. Inlet centerline temperatures for the tunnel and jets are conducted separately from the TR-PIV measurements due to their intrusive nature and are accomplished with the aforementioned type T thermocouples. Likewise, in order to protect the gas-dedicated sensor from seeder particle contamination, the gage pressure readings are conducted separately from the TR-PIV experiments and are provided by an Omega Engineering Model PX409-2.5CGUSBH compound gage pressure transducer. All gage pressure readings have been corrected for DC offset with the use of a preliminary measurement with the system completely off. The thermocouple measurements are recorded by a dedicated National Instruments NI 9213 data acquisition unit. All other probes use a National Instruments NI 9205 data acquisition unit, with the exception of the gage pressure sensor, which is directly mounted to the acquisition computer. All in-situ reference probes are sampled at 100 Hz for 10 s for each of the six repeatable TR-PIV experimental trials. The inlet temperature and gage pressure measurements are sampled at 100 Hz and 1 kHz, respectively, for 5 s and one trial each. Total uncertainties for each sensor and corresponding metric(s) are calculated as described in Sect. 2.2., consisting of repeatable trials where applicable for the random contribution and systematic uncertainties according to manufacturer specifications and conventional measurement uncertainty theory (Figliola et al. 2011). All reference measurements and corresponding uncertainties are available in Appendix (Tables 3 and 4).

### 3 Results

The investigation consists of TR-PIV measurements in the  $xy$  and  $xz$ -plane. The  $xy$  measurements provide jet exit conditions, first and second order turbulent statistics and several parameters related to the conventional jet in crossflow including streamline trajectories, recirculation areas and penetration depths. The  $xz$  measurements provide an optimal plane for POD, from which the single and tandem jet modes are examined. The truncated modes are used to reconstruct

the velocity components and vortex identification algorithms are employed to provide several vortex statistics in the spanwise plane.

### 3.1 $xy$ plane measurements

#### 3.1.1 Inlet profiles

The authors were especially critical of the resulting velocity vectors near the jet exits and in preparing the resulting jet exit velocity profiles. Typical limitations and concerns for PIV in these regions include seeder particles coming from off-camera (inside pipe) to on-camera (visible in test section), unwanted noise from incident laser light on the ceiling of the test section or jet tubes and for the transverse jet, the added complexity of highly three-dimensional momentum exchanges that begin upstream of the exit plane inside the pipe. The current work also seeks to benefit from the direct comparison of exit velocity profiles provided by both the free and transverse jet formations, i.e., without and with the presence of a crossflow, respectively. Under these constraints, the first mutually accessible exit profiles were resolved at  $y=7.58$  mm from the jet exits ( $y=0$  mm) for both the free and transverse profiles. These profile locations also ensure that the corresponding turbulent kinetic energy estimates are accurate (Tables 3 and 4 in Appendix), i.e. not susceptible to incident laser light on the nozzle exits. Jet exit velocity profiles are presented in Fig. 3 for both the free and transverse jet formations, i.e., without and with the presence of a crossflow, respectively. The free jet velocity profiles in Fig. 3a, b and c show excellent agreement in both magnitude and shape at a given flow rate. Each of the free jet profiles also exhibits self-similarity, as expected. The free jet velocity inlet profiles ensure a good basis for comparison between the single and tandem jet formations at each of the proposed jet to crossflow velocity ratios.

As expected, the transverse jet inlet profiles in Fig. 3d, e and f, exhibit dramatically different inlet profiles as a result of the varying influence of the crossflow on each jet. Several observations are immediately clear, the first of which is the transfer of momentum to the streamwise component,  $\langle U \rangle$ , from the transverse jet direction,  $\langle V \rangle$ . Though not directly quantified, it is appreciable to recognize that this effect is also present in the out-of-plane velocity component,  $\langle W \rangle$ . Andreopoulos et al. (1984) originally described this behavior for a single jet in crossflow as being analogous to partially covering the exit of a free jet. It is well understood that the bending of the jet begins upstream of the jet exit ( $y/D < 0$ ). The behavior is further complicated by the jet's interaction and stalling of the crossflow on its windward side, separating its oncoming boundary layer and initiating the horseshoe vortex. Jet 1 is the most reminiscent of the single jet, having nearly identical  $\langle U \rangle$  profiles across all examined

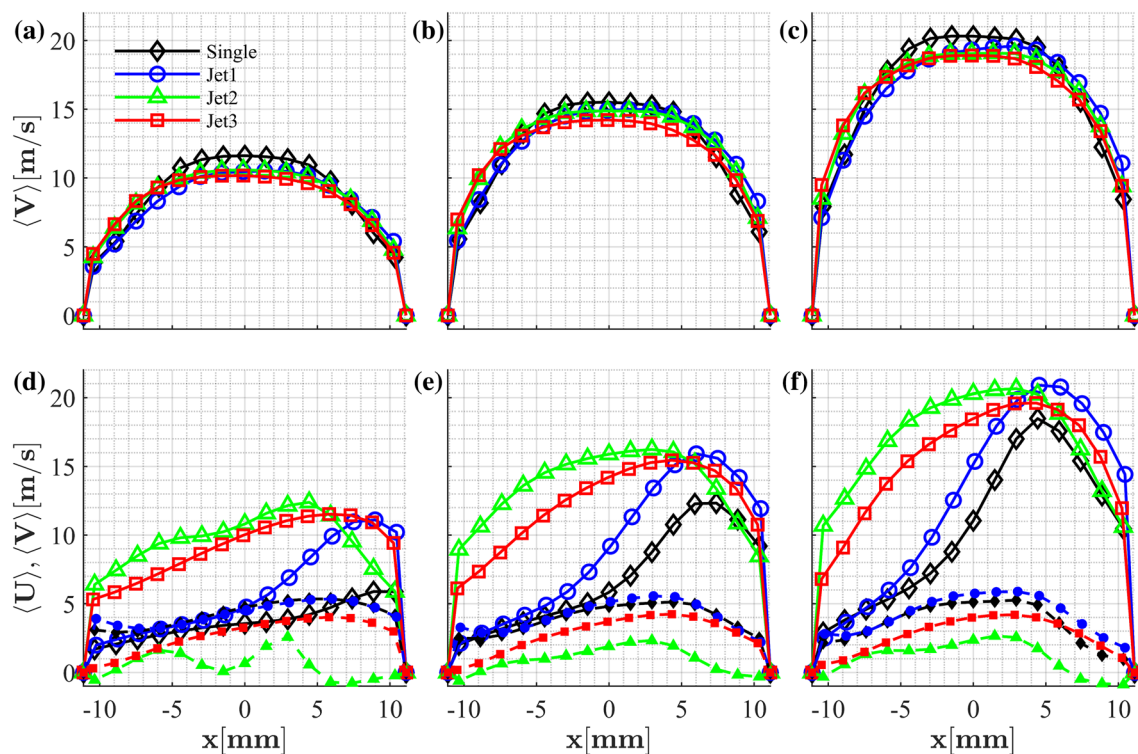


**Fig. 3** a–c Free jet and (d–f) jet in crossflow outlet velocity profiles. Columns (from left to right) indicate  $V_j/U_\infty=0.9, 1.25$  and  $1.7$ . Filled and unfilled markers indicate ensemble averaged streamwise  $\langle U \rangle$  and transverse  $\langle V \rangle$  velocity components, respectively

cases. Interestingly, jet 1 has a slightly higher  $\langle V \rangle$  than the single jet for a given case and this difference is diminished with increasing  $V_j/U_\infty$  and the single jet recovers the same profile as jet 1. This is believed to be caused by the downstream jet 2 and possibly jet 3, that provide some contribution upstream, most likely a reduced pressure region, on the leeward side of jet 1. Several tandem twin jet studies typically observe the “shielding” effect of the upstream jet on that of the downstream one (Gutmark et al. 2011; New et al. 2015). An additional insight here lies in the rear shielding, or exchange, between the second and third jet. Jet 2 exhibits higher magnitude  $\langle V \rangle$  profiles across all available cases.

### 3.1.2 Instantaneous and time-averaged velocity fields

Instantaneous velocity magnitude,  $U_{mag}$ , fields and corresponding vector components are displayed in Fig. 4a, b, c, d, e and f for the single and tandem jets, respectively, at each velocity ratio depicting the unsteady features of the flows. The classical single round jet reveals the well-known shear layer instabilities and wake formations found on the windward and leeward side of the jet, respectively. Evolution of the shear layers are strongly a function of velocity ratio, where for low velocity ratios, it has been confirmed that the shear vortices produced by these layers dominate those produce by the wake (Meyer et al. 2007). The instantaneous

fields also reveal the downstream effects of the flow separation that occurs inside the jet pipes, as examined previously in the velocity exit profiles from Fig. 3d, e and f. As a result of mass conservation, the jets are shifted towards their leeward side (Kelso et al. 1996; Muppidi et al. 2005). The leading jet in the tandem formation is found to exhibit qualitatively similar features as the single jet, though its downstream counterparts penetrate much deeper into the flow and exhibit complicated shear layer and wake interactions. With increasing velocity ratio, the downstream jets penetrate deeper into the crossflow and exhibit features more reminiscent of free jets, particularly in the near field region of jet 2 in Fig. 4e and f and reaffirmed by the exit profiles found in Fig. 3e, f as they reach a parabolic state.

The ensemble averaged velocity magnitudes,  $\langle U_{mag} \rangle$  and corresponding vector components are displayed in Fig. 5a–f for the single and tandem jet configurations, respectively, for each velocity ratio. Figure 5a–c provides the classical observations of the jet bending into the crossflow, increasing in width downstream, wider on its leeward side than its windward side and a sharp decrease in velocity magnitude directly behind the jet. In Fig. 5d–f, each of the tandem jets provides a unique display of these same observations, with jet 2 and jet 3 showing exacerbated widths and penetration depths compared to the leading jet 1 or the single jet from Fig. 5a–c.



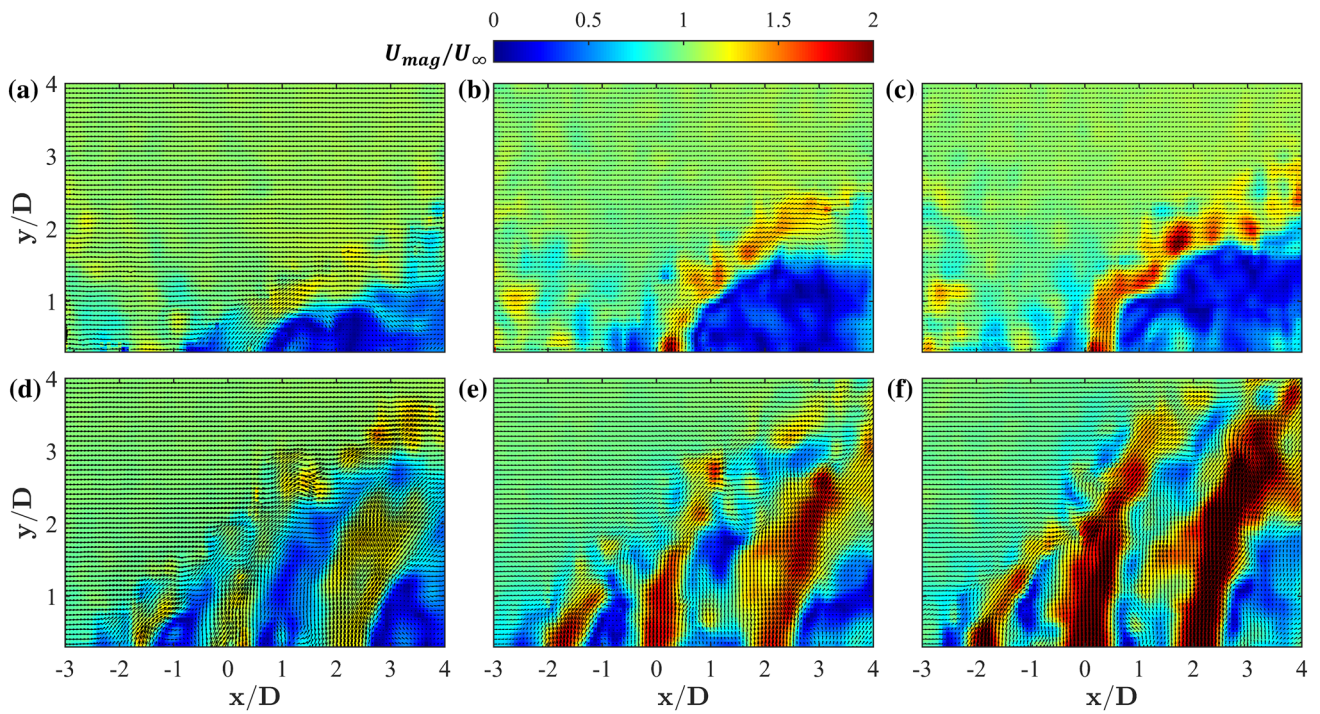


**Fig. 4** Instantaneous velocity magnitudes,  $U_{mag}/U_\infty$ , contours for (a-c) single and (d-f) tandem jet at  $V_j/U_\infty=0.9, 1.25, 1.7$  as seen in first, second and third column, respectively

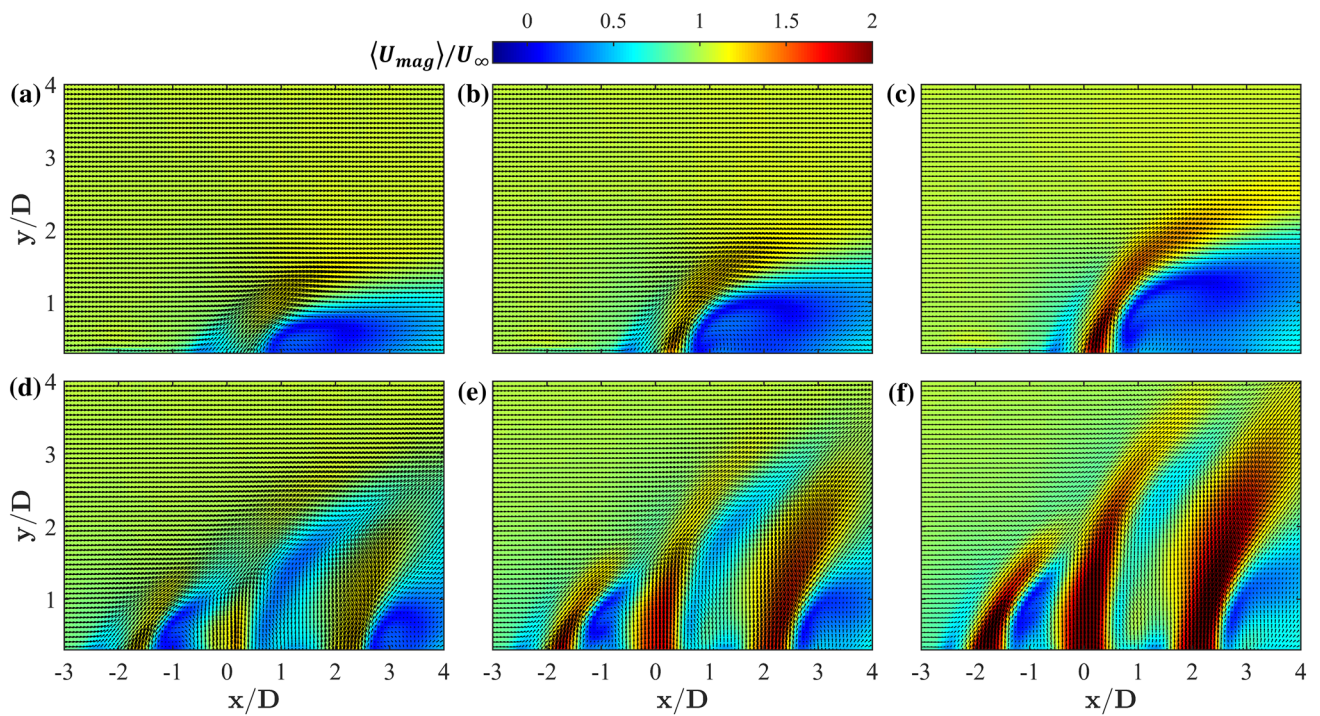


**Fig. 5** Ensemble-averaged velocity magnitude,  $\langle U_{mag} \rangle / U_\infty$ , contours for (a-c) single and (d-f) tandem jet at  $V_j/U_\infty=0.9, 1.25, 1.7$  as seen in first, second and third column, respectively

Several complicated interactions inhibit or strengthen the velocity magnitudes directly behind each jet as well, as a result of the tandem configuration, competing pressure effects and vortex formations found in these regions.

Ensembled averaged streamwise,  $\langle U \rangle / U_\infty$  and transverse,  $\langle V \rangle / U_\infty$ , velocity profiles and corresponding uncertainties are presented in Fig. 6a–d for the single and tandem jets, respectively. The profiles provide further insight into the development of each jet's contribution to the momentum in the positive  $y$ -direction as a function of increasing distance downstream in the  $x$ -direction. Decreasing magnitudes in  $\langle V \rangle$ , with downstream distance indicates a transfer of momentum to the dominant streamwise freestream velocity,  $\langle U \rangle$  and to a lesser extent, the spanwise ( $W$ ) direction of the jets, examined further in Sect. 3.2. The highest velocity ratio provides the largest variation in profile magnitudes and span, yet across all cases, the same general trends are confirmed for the single and tandem jet cases, respectively. Immediately positive regions of  $\langle V \rangle$  at each jet axial line trace indicate the direct near field effects of the jet penetration. Strong decreases in  $\langle V \rangle$  are indicative of the flow reversal caused by adverse pressure gradients and corresponding wake vortices which are reaffirmed by steep gradients in  $\langle U \rangle$ . Secondary maxima in  $\langle V \rangle$  are the result of the mean shear prompted by the jet to crossflow interactions, which are further amplified by the introduction of additional jets downstream.

### 3.1.3 Jet trajectories, recirculation areas and penetration depths

In typical jet in crossflow studies, the jet trajectory is determined according to the path of maximum ensemble-averaged velocities in the  $xy$ -plane (Gutmark et al. 2011). The TR-PIV measurements produce local maxima, particularly in the near field of the jet exits and the same behavior has been confirmed previously by Yuan et al. (1998) in their LES simulations. The authors proposed the use of streamline trajectories originating from the centroid of the jet exit, which has the added advantage of a full field trajectory throughout the entire velocity field. This method is followed to the extent possible, with the caveat that TR-PIV measurements are not resolved directly at the jet exit as stated in Sect. 3.1.1. Thus, the streamlines originate at the centerline of each jet:  $x/D = -2, 0$  and  $2$  for jets 1, 2/single and 3 and at the  $y/D = 0.34$  downstream location. An example of the full field streamlines and highlighted jet trajectories are presented in Fig. 7a and b, for the single and tandem jets, respectively at  $V_j/U_\infty = 1.7$ . It is clear that the tandem jet configuration exhibits deeper penetration into the crossflow than that of the single jet. The recirculation regions, defined by the lines of zero streamwise iso-velocity, behind each jet are also highlighted in Fig. 7a, b. It is immediately apparent that each of the jets exhibit a unique recirculation shape.

Scaling analysis for the single round jet in a crossflow has historically employed a power law fit to describe collapsed trajectories with one of the earliest known attempts

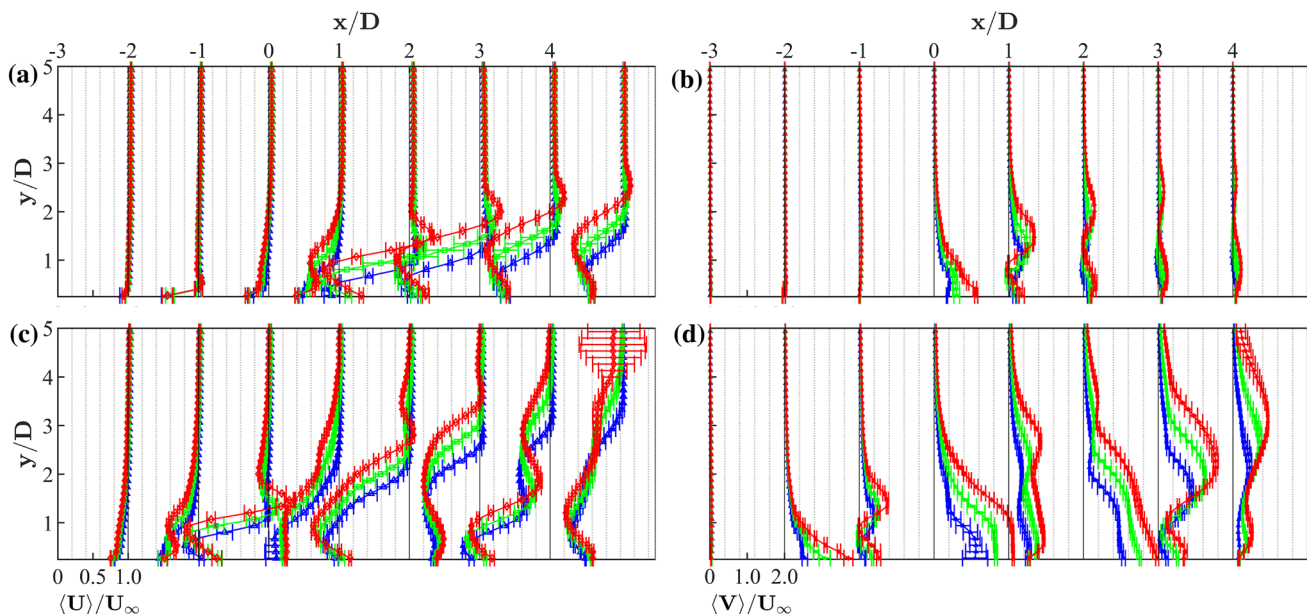
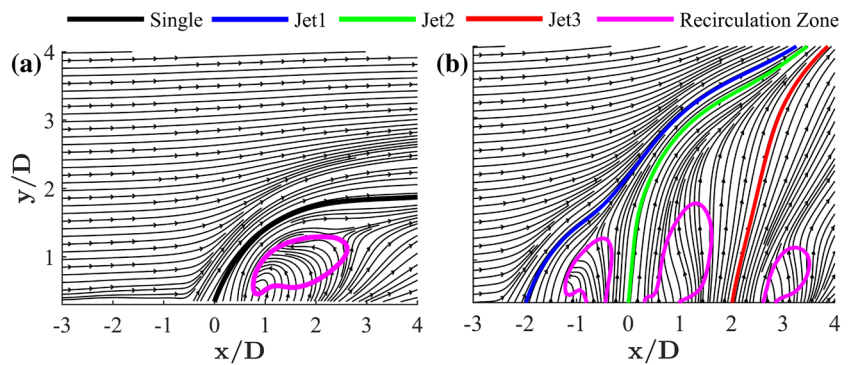


**Fig. 6** Ensembled-averaged velocity profiles (a, c)  $\langle U \rangle / U_\infty$  and (b, d)  $\langle V \rangle / U_\infty$  with total uncertainties. Rows (top to bottom) correspond to single and tandem jet configurations. Legend: Colors/shapes indicate

$V_j/U_\infty = 0.9$  (blue triangles),  $V_j/U_\infty = 1.25$  (green squares) and  $V_j/U_\infty = 1.7$  (red diamonds)



**Fig. 7** **a** Single and **(b)** tandem jet ensemble-averaged velocity streamlines at  $V_j/U_\infty=1.7$  with centerline trajectories and recirculation zones highlighted



provided by Pratte et al. (1967). A universal collapse and a robust regression model for the jet in crossflow has proven to be elusive, as the behavior is strongly a function of the characteristic flow ratio and in turn, the boundary layer interactions and vortex mechanisms present. An excellent look at these transition processes at low velocity ratios ( $0.15 < V_j/U_\infty < 2.2$ ) is provided by Cambonie et al. (2014). These authors have also identified the characteristic flow ratio, jet diameter and boundary layer as critical variables towards a universal scaling function (Cambonie et al. 2013). Scaling of the current results are briefly examined here. Figure 8 provides streamline trajectories for all of the available test cases. Each of the jets' respective positions have been collapsed onto a generic centerline origin ( $x/D=0$ ). Figure 8a and b utilized ' $rD$ ' and ' $r\delta$ '-scaling, respectively, the two most fundamental scaling methods found in the jet in crossflow literature. It should be noted that ' $r$ ' in the jet to crossflow literature may refer to the velocity (as in here) or momentum ratio, however to avoid confusion in subsequent sections, the current study defines this variable explicitly as  $V_j/U_\infty$ . Additionally, the boundary layer thickness,  $\delta$ , is defined locally for each jet as discussed in Sect. 2.1. From comparison of Fig. 8a and b it is clear that the  $(V_j/U_\infty)\delta$  scaling provides a better collapse of the tandem jet trajectories and that neither scaling sufficiently collapses the single jet trajectories onto the tandem ones. The quest for universal scaling is further complicated by the inclusion of additional tandem jets. New et al. (2015) have studied the twin tandem jet with variable

spacing in the range  $1.5-3 D$  and velocity ratios between  $2 < V_j/U_\infty < 8$ . They observed that the merged trajectories of the tandem jet configuration penetrated deeper into the crossflow than their analogous single jet counterparts. The authors reason that the increased freestream penetration is a result of the shielding and merging of the twin tandem jets which is strongly function of their separation distance. Utilizing their profiles and those of a similar twin tandem jet study by Gutmark et al. (2011), the authors proposed a modified ' $rD$ '-scaling assuming a virtual origin at the mid-point between the upstream and downstream jets and the use of an 'effective' velocity ratio for the tandem jets. With the onset of several (greater than two) tandem jets at low velocity ratios, as in the current results, the interaction of the encapsulated (middle) jet promotes new shielding interactions that will require further analysis of existing scaling laws beyond the current investigation's scope. These considerations will be most readily assessed with a larger velocity field than that currently available and with a wider range of velocity ratios tested, suggesting an auspicious route for analogous computational modeling of the tandem jets.

Flow reversal regions for each jet and velocity ratio are presented in Fig. 9 and are collapsed according to the same generic centerline criteria described previously for Fig. 8. For a single jet configuration, an adverse pressure gradient forms directly behind the jet column, obstructing the crossflow and forcing it into this recirculation region on the leeward side of the jet. The recirculation region induces a

**Fig. 8** Collapsed jet centerline trajectories for all available jet and velocity ratio configurations according to **(a)** ' $rD$ ' scaling and **(b)** ' $r\delta$ ' scaling. Circle, triangle and square markers indicate  $V_j/U_\infty=0.9, 1.25, 1.7$ , respectively. Black, blue, green and red colors denote single jet, jet 1, jet 2 and jet 3, respectively

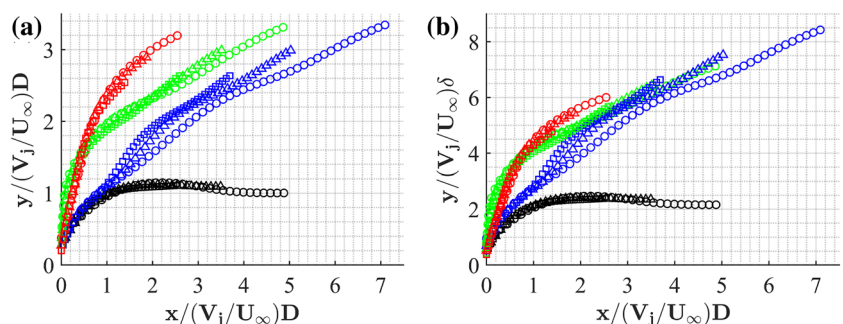
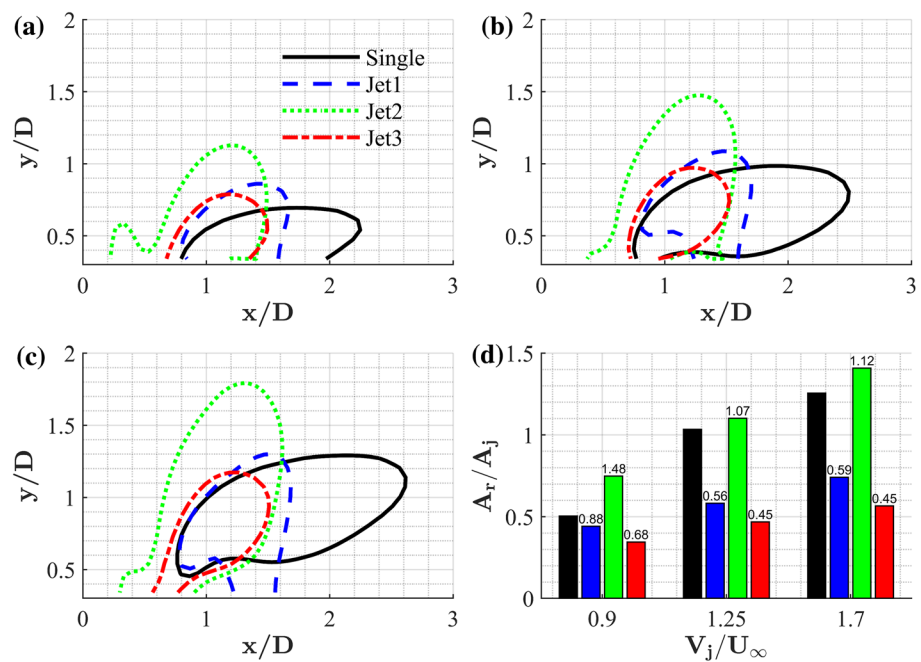


**Fig. 9** Collapsed recirculation regions behind each jet for (a)  $V_j/U_\infty=0.9$ , (b)  $V_j/U_\infty=1.25$  and (c)  $V_j/U_\infty=1.7$  and (d) recirculation zone areas for each jet and velocity ratio. Note: Number labels in (d) indicate ratio of entry over respective single jet entry in grouping



lifting force that enhances the jet trajectory away from the upper wall. For adjacent tandem jets, the downstream jet has an additional blockage that yields a larger adverse pressure gradient behind the upstream jet, thereby leading to a higher recirculation area as observed previously by Gutmark et al. (2011). The authors found that the reverse flow region behind the front jet is somewhat larger than that of the corresponding single jet case and that the recirculation region behind the rear jet is nearly eliminated. It should be noted that the authors utilized ‘ $rD$ ’ scaling, contrary to the current study non-dimensionalizing explicitly by  $D$ . Contrary to their findings, the recirculation regions behind the second and third jets are comparable in size to both the single jet and leading jet 1 for each of the velocity ratios as depicted in Fig. 9a, b and c. By collapsing the profiles, it is clear that all four jets exhibit shared regions (overlap) and unique shapes outside of these regions. In particular, jet 2 exhibits a substantially larger recirculation zone than any of the other jets, further exemplifying the exchange of shielding and the effects of adverse pressure for tandem jet arrays. Though resolution of the near wall recirculation is excluded, the current results are admissible for a basic order of magnitude assessment, pictured in Fig. 9d where the area of recirculation,  $A_r$ , for each jet is non-dimensionalized by the area of the jet exit,  $A_j$ . These results are subject to some level of scrutiny, where again, measurements closer to the wall would promote slightly larger areas. From Fig. 9d, each recirculation region increases as a function of increasing velocity ratio. Across all available measurements, the largest recirculation areas are found in jet 2 and the smallest in jet 3. This promotes an interesting finding and supplement to

the original observations of Gutmark et al (2011). While jet 3’s recirculation is in no way eliminated, it is substantially lower than the single jet or jet 1. Additionally, at the lowest velocity ratio ( $V_j/U_\infty=0.9$ ) jet 2’s recirculation zone is considerably larger ( $\sim 50\%$ ) than that of the analogous single jet case. Yet with increasing velocity ratios, jet 2 and the single jet approach nearly identical values, with jet 2 still being slightly larger.

Given the high spatio-temporal content of the TR-PIV measurements, the instantaneous penetration depths can be directly quantified for each jet. The penetration depths are defined here as the maximum transverse velocity gradient between two neighboring vectors along an arbitrary jet axial centerline, i.e. where  $dV/dy$  is maximum. These values are computed for each jet’s axial centerline and each velocity ratio tested and consolidated in Fig. 10. The central line of each box indicates the median and the bottom and top edges represent the 25 and 75% of the data, respectively. The whiskers correspond to approximately 2.7 standard deviations or 99.3% coverage of the data, here assumed to be normally distributed. Mean penetration depths,  $\mu_{y/D,i}$  for each jet are also reported. The single jet and jet 1 exhibit markedly similar mean and median penetration depths across all three velocity ratios. Reminiscent of previous observations from the jet trajectories and recirculation regions, the tandem penetration depths are also strongly a function of velocity ratio and present a general hierarchy of increasing depth for each additional jet downstream, i.e.  $\mu_{y/D,J1} < \mu_{y/D,J2} < \mu_{y/D,J3}$ . Interestingly, for the velocity ratio below unity ( $V_j/U_\infty=0.9$ ), jet 2 exhibits mean and median penetration depths similar



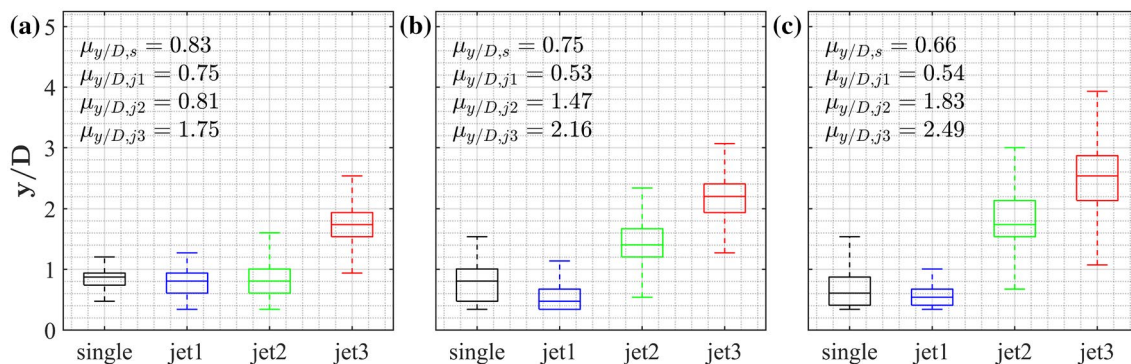


**Fig. 10** Summary statistics of instantaneous penetration depths for each jet corresponding with (a)  $V_j/U_\infty=0.9$ , (b)  $V_j/U_\infty=1.25$  and (c)  $V_j/U_\infty=1.7$ . Legend: Colors are consistent with Fig. 9

to the single jet and jet 1. Regarding the velocity ratios greater than one, ( $V_j/U_\infty=1.25$  and  $1.7$ ) jet 2 mean and median penetration depths are almost directly in between (halfway) that of jet 1 and jet 3, but exhibit nearly identical amounts of variation (seen as the whiskers) as that of jet 3. While the steady penetration depth found for jet 2 may be unsurprising, the variations found for the encapsulated jet 2 below and above  $V_j/U_\infty=1$  have important consequences in turbulent mixing and control.

### 3.1.4 Reynolds stresses

Ensembled-averaged Reynolds shear stress,  $\langle u'v' \rangle / U_\infty^2$ , profiles are presented in Fig. 11a, b, c, d, e and f for the single and tandem jet configurations, respectively, at each velocity ratio. From Fig. 11a it is clear that the single jet at the lowest velocity ratio provides the simplest set of features depicting the shear stress. Beyond the immediate wall region ( $y/D=0$ ), the positive shear is very weak and a pocket of relatively high negative shear exists in the wake. With increasing velocity ratios found in Fig. 11b, c the positive

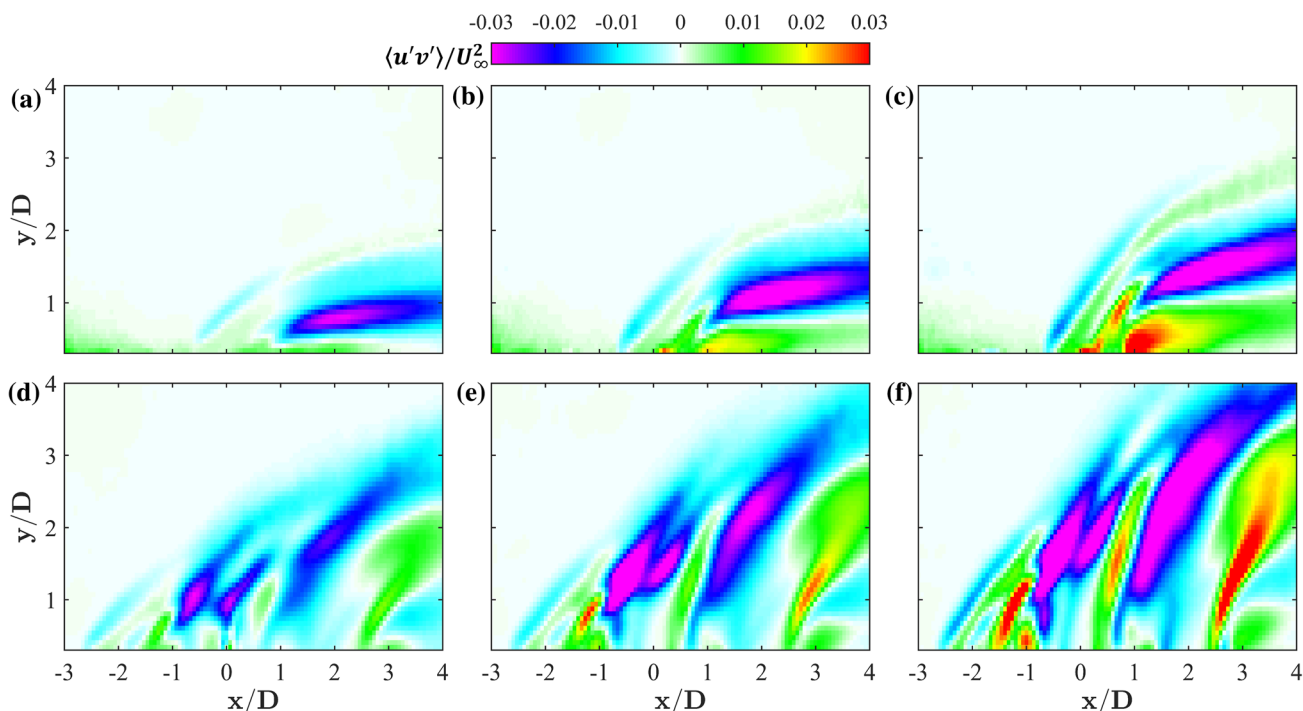


**Fig. 11** Reynolds shear stress,  $\langle u'v' \rangle / U_\infty^2$ , contours for (a–c) single and (d–f) tandem jet at  $V_j/U_\infty=0.9, 1.25, 1.7$ , as seen in first, second and third columns, respectively

and negative shear regions that comprise the jet core become clearer, seen as long streaks and resulting from the shear layers. The development of a high positive shear region in the wake can be seen immediately behind the jet exit in Fig. 11c and is believed to be the result of the exchange between the horseshoe and wake vortices. In general, the single jet's region of negative shear in the wake extends with the jet trajectory. As the jet bends into the freestream, this region is elongated in the  $x$  direction, but no longer increases in thickness. The tandem array found in Fig. 11 yields more localized or smaller regions of high positive shear and in general these regions are more prevalent than the single jet for each velocity ratio tested. The negative shear regions exhibit markedly different evolutions than their single jet comparisons. These regions extend much further in the positive  $y$  direction and less in the streamwise direction. For each velocity ratio tested, the initial negative shear region found between jets 1 and 2 splits into two smaller regions while the downstream region between jets 2 and 3 is more unified. The Reynolds shear stress isolates the velocity fluctuations and their corresponding effects on the flow induced stresses, but geometric, pressure and vortical considerations may also aid in prescribing these formations.

Reynolds shear stress profiles are presented in Fig. 12a and b for the single and tandem jets, respectively. The associated uncertainties are a function of the random component of uncertainty only. For PIV measurements, proper quantification of the systematic uncertainty of propagated statistics such as the Reynolds stresses is an ongoing challenge (Sciacchitano et al. 2015). For the single jet in Fig. 12a, the

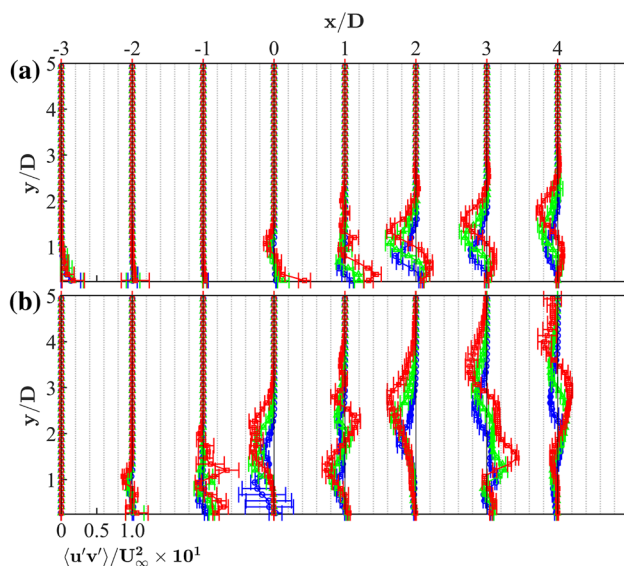


**Fig. 12** Ensemble-averaged Reynolds shear stress,  $\langle u'v' \rangle / U_\infty^2$ , profiles with random uncertainty for (a) single and (b) tandem jets. Legend: Colors/shapes indicate  $V_j/U_\infty = 0.9$  (blue triangles),  $V_j/U_\infty = 1.25$  (green squares) and  $V_j/U_\infty = 1.7$  (red diamonds)

$\langle u'v' \rangle$  shear stress reaches a maximum in the immediate exit region of the jet and exhibits a positive shear in the wake with corresponding negative shear at the interface with the free stream along the jet's trajectory. For the tandem jets, the first jet exhibits similar behaviors along its centerline at  $x/D = -2$  and immediately downstream at  $x/D = -1$  profile. This implies that the fluctuating velocity components and shear stresses in this intermediate region (between the leading and middle jet at  $x/D = -1$ ) is largely unaffected by the presence of the middle jet. At  $x/D = 0$  however, several new features are apparent. Negative values of shear stress develop along each jet axial centerline, namely,  $x/D = -2, 0$  and  $2$ , where each negative peak shows greater magnitude and spread than that directly upstream. A more interesting observation is found when comparing the intermediate profiles  $x/D = -1$  and  $1$ , to the profile just beyond the third and final jet at  $x/D = 3$ . The  $x/D = -1$  and  $x/D = 1$  profiles exhibit strong positive peaks as a result of the recirculation zones, with more complicated exchanges of positive and negative shear towards the outer shear layer interaction with free stream. This is in contrast to the hot-wire anemometry results of Isaac and Jakubowski (1985), who conducted single and twin tandem jet experiments that exhibited nearly identical mean velocities and Reynolds stresses across both jet configurations. The discrepancy is explained by the velocity ratios tested, where their experiments were conducted at  $V_j/U_\infty = 2$  and the profiles herein are all less than this value. It is reasonable then, to state that the turbulent/vortex mechanisms driving these behaviors are more unique and localized for velocity ratios less than 2. This statement is further supported by the transition behaviors present at low velocity ratios, as first revealed by Cambonie et al. (2014). The profiles found in the wake of the entire configuration, i.e.  $x/D = 3$  and  $4$ , reveal the artifacts of these exchanges that have progressed further down in the positive  $y$  direction, while showing the additional development promoted by the recirculation region behind jet 3, much closer to the wall ( $y/D = 0$ ). The evolution of each shear stress generated and their exchange with downstream distance and dissipation of energy into the crossflow are pertinent to understanding the mixing effects promoted by the introduction of each additional jet in the tandem configuration.

### 3.2 $xz$ plane measurements

#### 3.2.1 Instantaneous and time averaged velocity fields

The instantaneous velocity magnitudes for the  $xz$  plane measurements at the  $y/D = 1$  location are presented in Fig. 13a, b, c, d, e and f for the single and tandem jets, respectively. At the front of each leading upstream jet (the single jet and jet 1) is a clustered low velocity region. This results from the horseshoe vortex formation

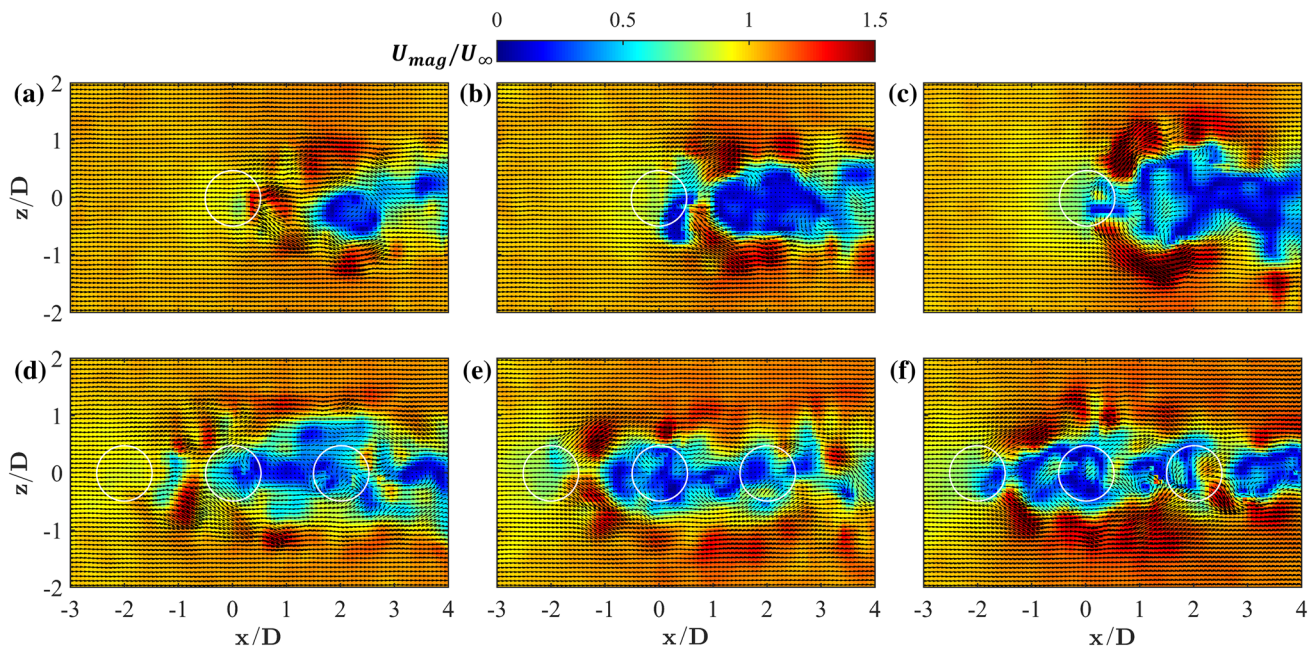


**Fig. 13** Instantaneous velocity magnitude,  $U_{mag}/U_{\infty}$ , contours with corresponding velocity vectors for (a–c) single and (d–f) tandem jets at  $V_j/U_{\infty}=0.9, 1.25, 1.7$  as seen in first, second and third column, respectively

as discussed previously. The interaction is initiated by the windward boundary layer and the adverse pressure gradient, which separates around the jet core, forming instabilities at the outer shear layers and spanwise vortices downstream (Mahesh 2013). This behavior has been previously determined to be periodic (Krothapalli et al. 1990), which will prove to be an attractive feature in subsequent sections. The vortex evolution in the positive  $x$ -direction is further complicated by the introduction of additional jets downstream and their repetitive features.

The ensemble-averaged velocity magnitudes at the  $y/D=1$  location are presented in Fig. 14a, b, c, d, e and f for the single and tandem jets, respectively and are briefly described here. For both the single and tandem configurations, clear symmetry is found across the  $z$ -axis, ensuring a general periodic motion for both the  $U$  and  $W$  components of velocity. From Fig. 14a, c it is clear that the single jet's wake region grows linearly with increasing  $V_j/U_{\infty}$  and goes from an elongated oval shape to an increasingly pronounced circular region best understood as the jet penetration out of the page. From Fig. 14d, e and f, it is evident that the introduction of each additional jet downstream yields a slightly different effect in its wake. For the lowest velocity ratio in Fig. 14d, it appears that jet 2 has the most pronounced low velocity region, while the leading jet is the victor for the  $V_j/U_{\infty}>1$  cases in Fig. 14e and f.

### 3.2.2 Proper orthogonal decomposition

With key features of the  $xz$  plane velocity fields addressed, the instantaneous  $U(x, z, t)$  and  $W(x, z, t)$  velocity component flow fields are now examined via POD. The POD aims to identify the statistically dominant flow structures found in each of the velocity components, providing insight into the flow dynamics and potential scalar (heat, chemical, etc.) transport found in the spanwise formation of the single and tandem jets. The influence of the shear layer and wake vortices entice recurring eddies in the wake of each jet. The current POD examination will seek to first characterize these dominant forms and then upon reconstruction of the velocity fields, quantify the suppression of developed vortices promoted by the tandem array compared to the single jet at low velocity ratios.

The POD or Karhunen-Loève decomposition was introduced by Lumley (1967) and has become an essential tool in both high fidelity experimental and numerical fluid mechanics. The POD provides a low dimensional basis via modal decomposition of an ensemble of data, here applied to both velocity components  $U(x, z, t)$  and  $W(x, z, t)$ . An attractive property of the POD is its optimality, which provides the most efficient means of capturing the dominant characteristics of an infinite-dimensional process via a finite number of modes (Holmes et al. 1996; Sirovich 1987). This implies that the original data, i.e. the velocity fields  $U_i(x, z, t)$ , can be



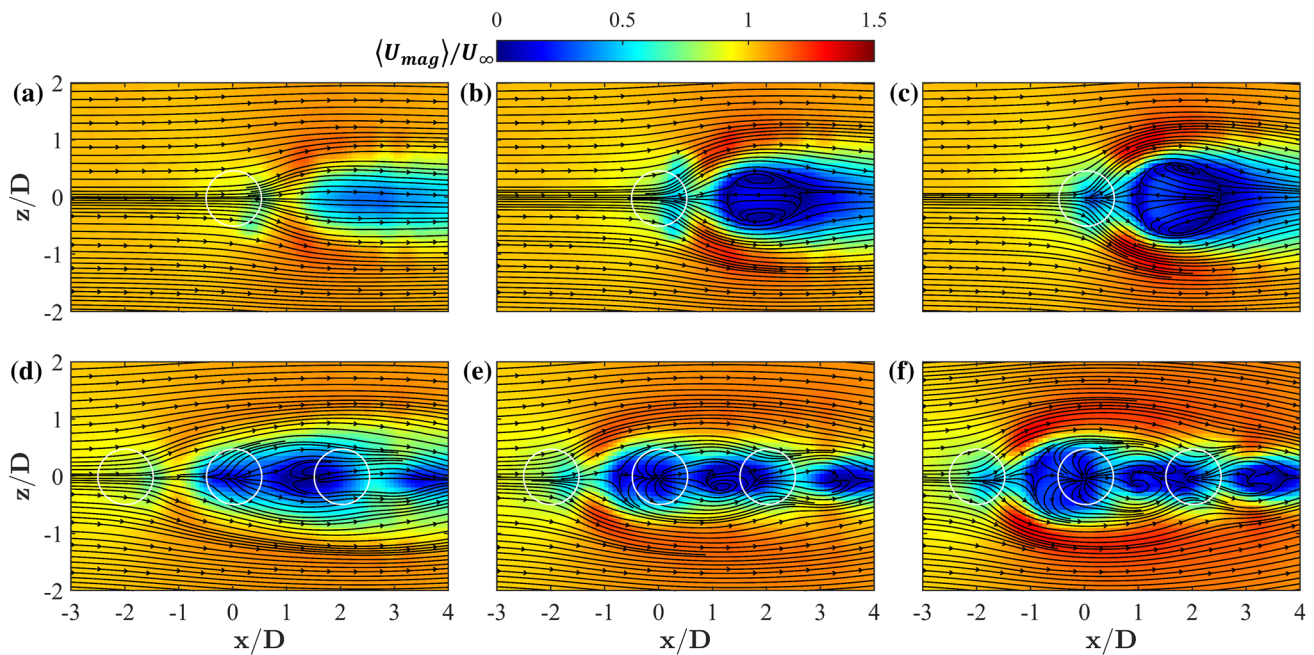


**Fig. 14** Ensemble-averaged velocity magnitude,  $\langle U_{mag} \rangle / U_\infty$ , contours with corresponding velocity streamlines for (a–c) single and (d–f) tandem jets at  $V_j/U_\infty=0.9, 1.25, 1.7$  as seen in first, second and third column, respectively

accurately approximated by only using the low order modes, containing the highest kinetic energy of the flow. The singular value decomposition method is utilized and briefly reviewed here using the convention of Brunton et al. (2019) and Taira et al. (2017).

The data set,  $\mathcal{X} \in \mathbb{R}^{n \times m}$ , here pertaining to velocity components  $U(x, z, t)$  or  $W(x, z, t)$ , is first organized into columns according to Eq. (1).

$$\mathcal{X} = \begin{bmatrix} | & | & \dots & | \\ x_1 & x_2 & \dots & x_m \\ | & | & \dots & | \end{bmatrix} \quad (1)$$

The reshaped data set consists of column vectors of the fluid velocity, where  $n$  is the number of discrete vector points in a given frame and  $m$  is the number of snapshots, in the data set. The singular value decomposition (SVD) of data matrix  $\mathcal{X} \in \mathbb{R}^{n \times m}$  is formulated according to Eq. (2).

$$\mathcal{X} = \Phi \Sigma \Psi^T \quad (2)$$

where  $\Phi \in \mathbb{R}^{n \times n}$ ,  $\Psi \in \mathbb{R}^{m \times m}$  and  $\Sigma \in \mathbb{R}^{n \times m}$  and where  $m < n$  for TR-PIV measurements and  $T$  is the transpose. Matrix  $\Sigma$  consists of real, non-negative entries along its diagonal and zeros everywhere else. Given that  $n > m$ , matrix  $\Sigma$  has a maximum of  $m$  non-zero elements along its diagonal. It is useful then, to employ the economy SVD to exactly represent  $\mathcal{X}$  according to Eq. (3).

$$\mathcal{X} = \Phi \Sigma \Psi^T = \begin{bmatrix} \hat{\Phi} & \hat{\Phi}^\perp \end{bmatrix} \begin{bmatrix} \hat{\Sigma} \\ 0 \end{bmatrix} \Psi^T = \hat{\Phi} \hat{\Sigma} \Psi^T \quad (3)$$

where  $\hat{\Phi}$  implies the economy-sized decomposition of the matrix (zeros removed),  $\perp$  is the orthogonal complement and hence, the columns of  $\hat{\Phi}^\perp$  and  $\hat{\Phi}$  span vector spaces that are complimentary and orthogonal. Matrices  $\hat{\Phi}$  and  $\Psi$  are unitary matrices consisting of orthonormal columns referred to as the left singular vectors and right singular vectors of  $\mathcal{X}$ , respectively. The columns of  $\hat{\Phi}$  are more formally known as the eigenvectors. The diagonal elements of  $\hat{\Sigma} \in \mathbb{R}^{m \times m}$  are the singular values, denoted by  $\sigma_1, \sigma_2, \dots, \sigma_m$  and are ordered from largest to smallest. For completeness, it should be stated that the singular values held in  $\Phi$  and  $\Psi$  are identical to the eigenvectors of  $\mathcal{X}\mathcal{X}^T$  and  $\mathcal{X}^T\mathcal{X}$ , respectively. Thus, the singular values are directly related to the eigenvalues,  $\lambda$ , via the relation  $\sigma^2 = \lambda$  (Taira et al. 2017).

From observation of Fig. 14, it is clear that the flows exhibit symmetry across the  $z$ -axis. This feature allows augmenting the data matrix  $\mathcal{X}$  for each velocity component. As suggested by Kutz et al. (2016) in their flow past a cylinder example, each data matrix is augmented with a secondary set of  $m$  snapshots, identical to the measurement data in  $\mathcal{X}$ , but flipped across the symmetric axis (here the  $z$ -axis) and corresponding sign change, according to Eq. (4).



$$\mathcal{X}_{aug} = \left[ \mathcal{X} - \begin{pmatrix} 0 & 0 & 1 \\ 0 & \cdot & 0 \\ 1 & 0 & 0 \end{pmatrix} \mathcal{X} \right] \quad (4)$$

The method is mathematically sound and still entirely a function of the observed physics; used as means of enforcing symmetry in the data set and strengthening signal correlation as a result of doubling the number of snapshots,  $m$ . As a final step before SVD computation, the velocity fields are non-dimensionalized beforehand and represent the instantaneous velocity, or non-mean subtracted data.

POD mode truncation is determined according to the optimal hard threshold criteria of Gavish et al. (2014). The criteria assumes that the data consists of Gaussian white noise of unknown magnitude with zero mean and unit variance. This method is well suited for experimental measurements where the noise level is unknown, in which the optimal hard threshold estimates the noise magnitude and scales the distribution of singular values according to the median. The singular values and cumulative energy distribution for the  $U(x, z, t)$  tandem jet data for each velocity ratio are displayed in Fig. 15a and b, respectively. The horizontal lines in Fig. 15a represent the optimal truncation cutoff  $\tau$  from which all singular values below this value are discarded. Likewise, in Fig. 15b, the vertical lines represent this same cutoff value, though here represented as the number of truncated modes,  $r$ .

From Fig. 15b the first mode only encompasses 29.4%, 26.2% and 22.6% of the cumulative energy for the  $V_j/U_\infty = 0.9, 1.25, 1.7$  cases, respectively. Each case exhibits a slow

increase in cumulative energy with the addition of each mode. A more heuristic approach to truncation may define a cutoff percentage for the cumulative energy, say 80%. From Fig. 15b, it is evident that 431, 500 and 589 modes are required by the  $V_j/U_\infty = 0.9, 1.25, 1.7$  cases, respectively. This slow convergence is best explained by the presence of small scale coherent structures in the flow, over which the kinetic energy is distributed. Nguyen et al. (2019a, b) have previously confirmed that for complicated wake formations, these small scale features are strongly a function of increasing Reynolds number, while here the same can be said for increasing velocity ratios. The observations found in Fig. 15 are in general, consistent across both velocity components and jet configurations. A full delineation of the truncation parameters for each velocity component of each velocity ratio and jet configuration are disclosed in Table 1, which highlights that the number of truncated modes,  $r$ , for the tandem jet is more strongly a function of  $V_j/U_\infty$  than that of the single jet, most reasonably understood as a result of an increase in kinetic energy and inherent noise associated with higher velocity ratios and additional turbulence generating devices (additional jets).

One of the earliest uses of POD on the single jet in cross-flow was performed by Meyer et al. (2007) who incorporated velocity ratios of 1.3 and 3.3 to determine that the low order modes are dominated by shear layer vortices and wake vortices, respectively. Across all velocity ratios in the current work, the mode shapes that most readily leverage these observations and provide the most beneficial insight are provided by the  $V_j/U_\infty = 1.7$  case. Low order eigenvectors for

**Fig. 15** **(a)** Singular values and **(b)** cumulative energy distributions for  $U(x, z, t)$  data at  $V_j/U_\infty = 0.9$  (blue), 1.25 (green) and 1.7 (red). Horizontal and vertical lines indicate the optimal singular value cutoff,  $\tau$  and modal truncation,  $r$ , respectively, for each case

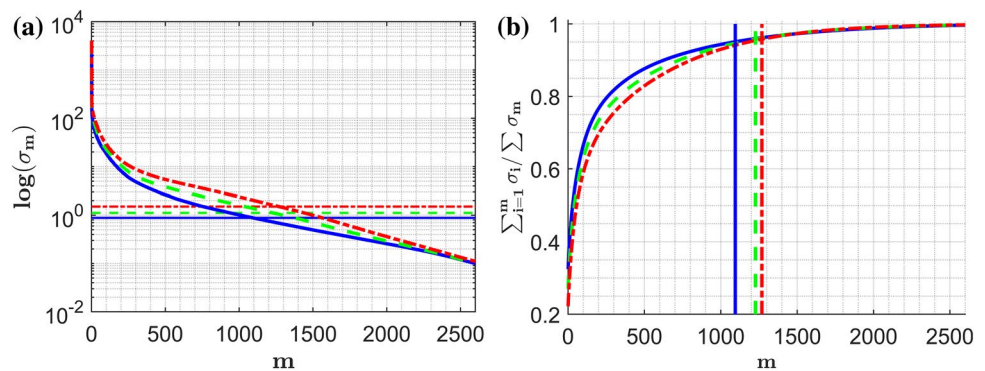


**Table 1** Optimal truncation parameters for each velocity component,  $U(x, z, t)$  and  $W(x, z, t)$ , associated with each jet configuration and velocity ratio tested

| $V_j/U_\infty$ | Single       |        |              |        | Tandem       |        |              |        |
|----------------|--------------|--------|--------------|--------|--------------|--------|--------------|--------|
|                | $U(x, z, t)$ |        | $W(x, z, t)$ |        | $U(x, z, t)$ |        | $W(x, z, t)$ |        |
|                | $r$          | $\tau$ | $r$          | $\tau$ | $r$          | $\tau$ | $r$          | $\tau$ |
| 0.9            | 1661         | 0.601  | 1557         | 0.624  | 1541         | 0.988  | 1514         | 0.999  |
| 1.3            | 1634         | 0.758  | 1557         | 0.770  | 1713         | 1.121  | 1646         | 1.155  |
| 1.7            | 1652         | 0.812  | 1569         | 0.871  | 1848         | 1.318  | 1747         | 1.408  |

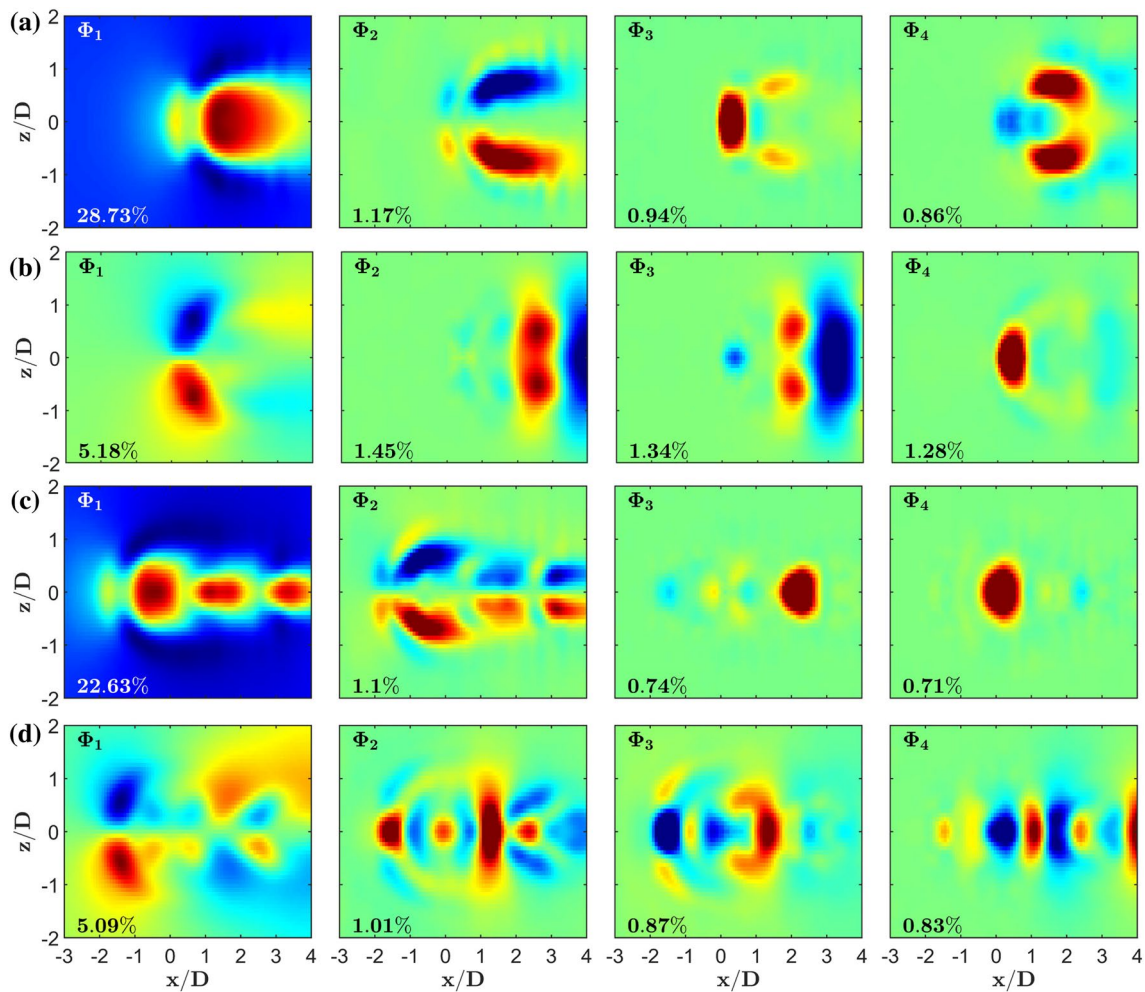


**Fig. 16** Low order POD eigenvectors with relative percent energy levels for the  $V_j/U_\infty=1.7$  (a, b) single and (c, d) tandem jets featuring velocity components (a, c)  $U(x, z, t)$  and (b, d)  $W(x, z, t)$

the single and tandem jet array at  $V_j/U_\infty = 1.7$  are displayed in Fig. 16a, b, c and d, respectively and feature both the streamwise and spanwise velocity shapes for comparison. Each of the first modes are qualitatively similar to the mean fields of their respective velocity components and capture the largest amount of relative kinetic energy as a result of the hierarchical ranking provided by the POD. The streamwise mode 1 is  $\sim 5.5$  and  $\sim 4.4$  times larger than the spanwise component for the single and tandem jet, respectively. The same notion can be extended to the inclusion of additional jets, as the streamwise mode 1 contribution for the single jet is  $\sim 27\%$  higher than that of the tandem array. The single jet streamwise mode 2 (Fig. 16a) exhibits an elongated “U”-shaped structure indicative of the outer shear layers of the jet. This same structure is present for each of the three tandem jets as seen in Fig. 16c and implies that the shear

layer vortices dominate the low order behavior as previously described for the single jet by Meyer et al. (2007). More localized features dominate the majority of the remaining modes, as a result of the periodic flapping of the jets and their respective core penetrations (larger oblong shapes) and wake vortices (smaller amorphous structures). In general, coherent structures are difficult to depict in high Reynolds number flows (Tables 3 and 4 in Appendix) and thereby the increased presence of turbulence. Regarding turbulent jets more specifically, several authors have confirmed additional challenges as a result of varying geometric configurations and flow conditions with notable examples included here. In their study of wall jets, another heavily streamwise dominated flow, Kaffel et al. (2016) utilized the POD and confirmed the presence of additional structures as the result of secondary instabilities in the spanwise direction. Likewise,



in their investigation of the jet in counterflow, Bernero and Fielder (2000) utilized the POD to find that when the periodicity of the jet is compromised, i.e. as a result of jet and counter flow strengths, low order coherent structures are less clear and a higher number of modes are required for reconstruction. Similar conclusions can be drawn in the current investigation, namely, the presence of secondary instabilities in the spanwise direction and the uncoupled periodicity of each jet as a function of velocity ratio and the effects of shielding. Further investigation of the phase behavior of the jet flows may provide additional insights into their coherent structures as discussed for free jets (Bonnet 1994) and pulsed jets (Vernet et al. 2009), though deemed beyond the scope of the current work. With that said, the current rendition of the POD is still advantageous for reconstruction and in the vortex identification that follows.

### 3.2.3 Vortex identification and statistical distributions

The truncated modes (Table 1) are projected onto the original TR-PIV measurement frames to produce POD modal reconstructions of the single and tandem jets in crossflow. Corresponding instantaneous and time-averaged vorticity contours and velocity vectors are presented in Fig. 17 and Fig. 18, respectively. The instantaneous velocity vectors provide some intuition into the small scale shear and swirl motions present in the flow. Small clusters of uni-directional velocity vector arrows are indicative of shear and highlighted with super-imposed straight magenta arrows in Fig. 17. Likewise,

pockets of rotating velocity vector arrows indicate the eddies in the flow field and are indicated with green rotating arrows in Fig. 17. The corresponding magnitudes of positive and negative vorticity found in Fig. 17 increase as a function of velocity ratio. The longer red and blue streaks are indicative of shear layer vortices (Kelvin–Helmholtz instabilities) which house the smaller wake vortices in between. It is also important to note that the tandem jet formations in Fig. 17d, e and f break up these shear layer streaks into smaller sections. The time-averaged velocity vectors in Fig. 18, reveal that the major shearing motions of the tandem jets are most prominent at the upstream jet 1 and are comparable in both size and direction to the single jet at an equivalent velocity ratio. Figure 18d, e and f reveal regions of little or no vortex magnitude, seen as the interstitial, crescent moon-shaped gaps found between the tandem jets. These time-averaged formations reaffirm the previous observations from Fig. 17d, e and f regarding the breakup of the shear layer streaks present in the tandem jet contours. The  $V_j/U_\infty = 0.9$  wake in Fig. 18d exhibits a much smaller gap in vortex formations between the upstream jet 1 and middle jet 2 than that found between jet 2 and the downstream jet 3. This is contradictory to the gaps found in the  $V_j/U_\infty = 1.7$  case of Fig. 18f which appear nearly identical in shape and relative location. It is reasonable then, to state that the vortices formed at these velocity ratios in the tandem jet array experience one or more transition processes predominantly as a result of velocity ratio and jet spacing. Regarding the velocity ratios, these observations are reaffirmed by the results of Cambonie

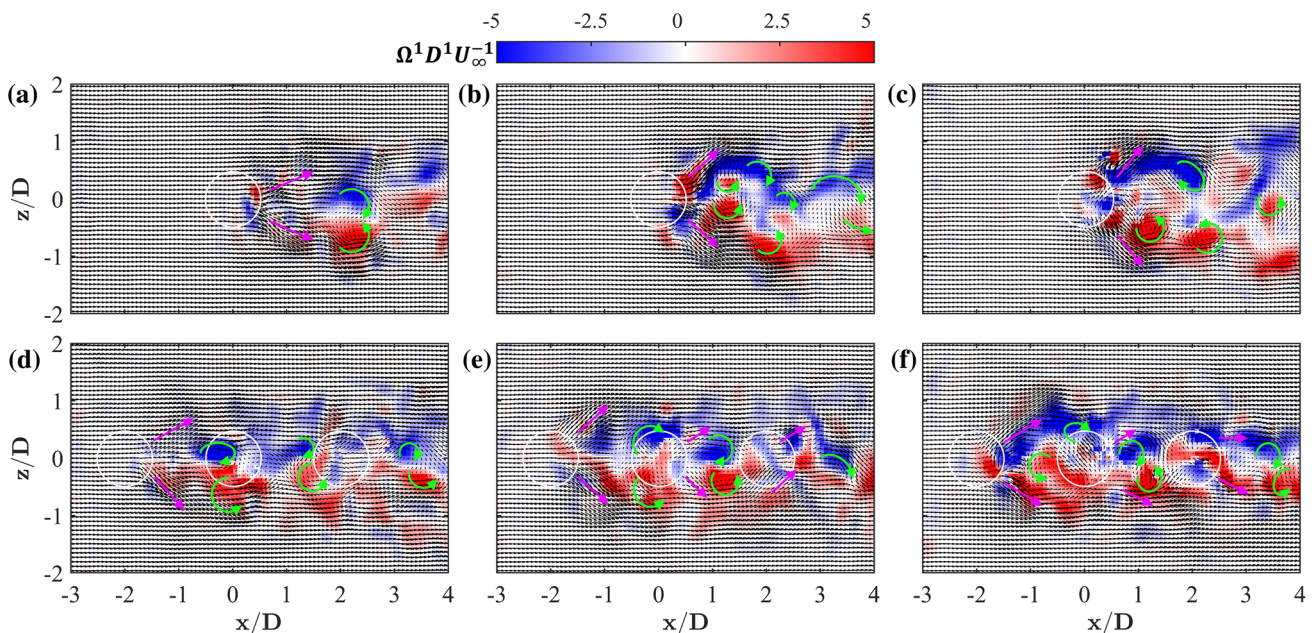


**Fig. 17** Instantaneous vorticity contours,  $\Omega^1 D^1 U_\infty^{-1}$ , with velocity vectors for (a–c) single and (d–f) tandem jets from POD reconstruction. Columns (from left to right) correspond to  $V_j/U_\infty=0.9, 1.25, 1.7$ , respectively

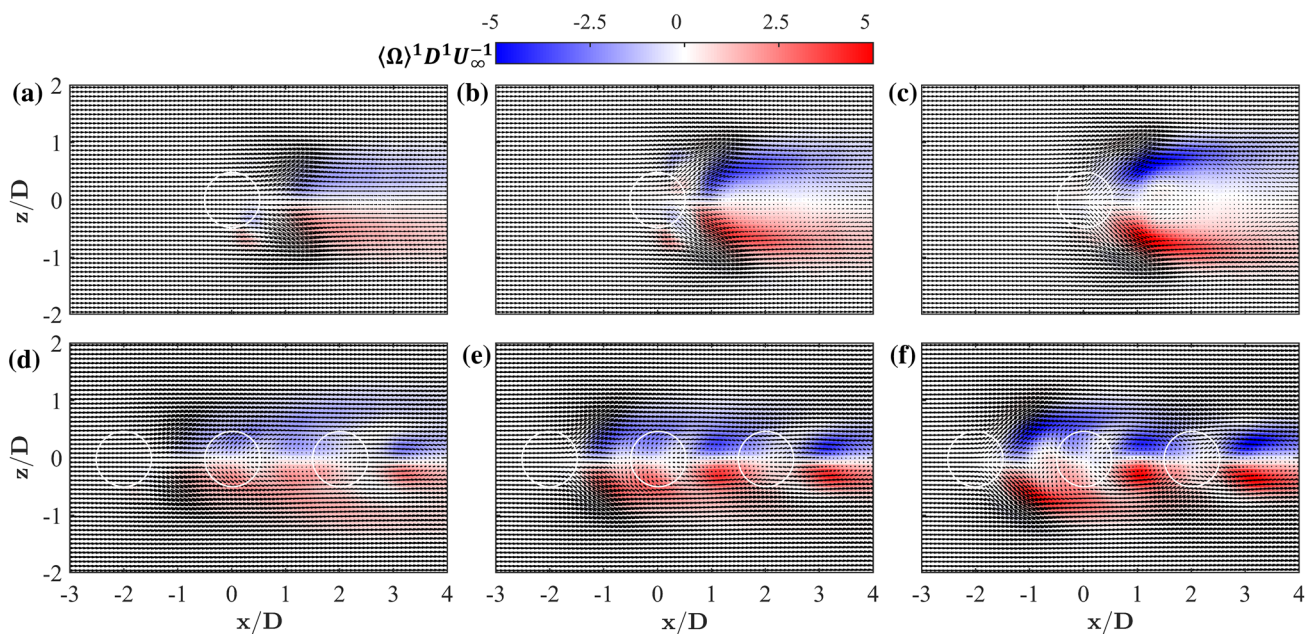


**Fig. 18** Ensemble-averaged vorticity contours,  $\langle \Omega \rangle^1 D^1 U_\infty^{-1}$ , with velocity vectors for (a–c) single and (d–f) tandem jets from POD reconstruction. Columns (from left to right) correspond to  $V_j/U_\infty=0.9, 1.25, 1.7$ , respectively

et al. (2014) who observed that the jet in crossflow experiences different process above and below a velocity ratio of  $V_j/U_\infty \approx 1.25$ . Though their results were based on the single jet in crossflow, comparisons between the current single jet and tandem jet formations in Fig. 17 and Fig. 18 allow for similar insight and comparisons to their study. In the range  $0.6 \leq V_j/U_\infty \leq 1.25$ , the jet is described as ‘detached’ with weak leading edge vortices and significant boundary layer interactions. For ratios above 1.25, the jet is described as ‘fully detached’, more indicative of classical jet in crossflow topologies, experiencing similar swirling strengths on the leading and trailing edge vortices and little to no interaction with the boundary layer. By capturing the single and tandem jet in crossflow below, above and directly at  $V_j/U_\infty=1.25$ , these vortex formations reveal the transitions processes in the  $xz$  plane for the tandem jets.

Further investigation of the vortical formations present in the single and tandem jet flows warrants the use of more robust identification algorithms. Several such methods exist and are broadly categorized as region- and line-based methods, integration- and geometry-based approaches, objective techniques, flow decompositions and optimization strategies, providing a wealth of techniques for interpreting rotational motion in fluid flows (Günther et al. 2018). The current work utilizes the region-based method of Graftieaux et al. (2001) in conjunction with the POD reconstructed instantaneous

velocity fields. For a given instantaneous velocity field, the vortex center is identified according the non-dimensional scalar function,  $\Gamma_1$ , which for a fixed point  $P$  in the discrete velocity field, is defined as

$$\Gamma_1(P) = \frac{1}{N} \sum_S \frac{(PM \wedge U_M) \cdot z}{\|PM\| \cdot \|U_M\|} = \frac{1}{N} \sum_S \sin(\theta_M) \quad (5)$$

where  $S$  is the rectangular domain of fixed size and geometry,  $M$  is a point inside  $S$ ,  $z$  is the normal vector of the measurement region,  $N$  is the number of points  $M$  inside  $S$  and  $\theta$  is the angle between velocity vector  $U_M$  and the radius vector  $PM$ .

The reconstructed fields have the added benefit of more clearly depicting the larger scale coherent structures, or energy containing energies, formed by the shear and swirl mechanisms, compared to the original instantaneous TR-PIV velocity fields which contain the effects of smaller velocity fluctuations from turbulence. According to Graftieaux et al. (2001), the scalar  $|\Gamma_1|$  is bounded by 1 and for swirling flows, reaches a value of 0.9 to 1 in the vortex center which is determined by a local maximum detection based on the appointed threshold. This threshold allows for removal of any remaining small-scale turbulent fluctuations. While the threshold is not Galilean invariant, it does provide an effective way of identifying vortex center



locations. The current investigation consists of several instantaneous swirling features, i.e. wake vortices, but as described previously, is not independent of the mechanisms of shear. Thus, an appropriate threshold value for the current study was found to be 0.75 from inspection of the instantaneous velocity fields and identified vortices. The second employed vortex algorithm incorporates a local convection velocity,  $U_p$ , to provide the vortex core identification found according to

$$\Gamma_2(P) = \frac{1}{N} \sum_S \frac{\left[ PM \wedge (U_M - \tilde{U}_P) \right] \cdot z}{\|PM\| \cdot \|U_M\|} \quad (6)$$

where  $\tilde{U}_P = (1/S) \int_S U dS$ , which in the context of discrete measurement fields, are approximated as the spatially averaged velocity components located in the measured domain  $S$  (with the exception of  $P$ ). For a 2D incompressible velocity field,  $\Gamma_2$  is a local function depending only on  $\Omega$ , the rotation rate corresponding to the antisymmetrical part of the velocity gradient  $\nabla u$  at  $P$  and  $\mu$ , the eigenvalue is the symmetrical part of the tensor. The authors then prove that  $|\Omega/\mu| > 1$  and  $|\Gamma_2| > 2/\pi$  when the flow is dominated by rotation. These values are adopted here as thresholds for the vortex core region and for estimation of the vortex area and circulation of all identified vortices.

The single and tandem vortex center locations, relative sizes and circulations are presented in Fig. 19 using the statistical characteristics promoted by Nguyen et al.

(Nguyen et al. 2019a, b; Nguyen, White, Vaghetto and Hassan 2019a, b). From examination of the single jet profiles in Fig. 19a, b and c, the total number of detected vortices,  $N_\Omega$ , is much smaller for  $V_j/U_\infty < 1$  than for the  $V_j/U_\infty > 1$  cases. With increasing values of velocity ratio above unity, the jet momentum in the transverse  $y$  direction (into the page in Fig. 19) overcomes and stalls the crossflow and contributes to an adverse pressure gradient behind the immediate jet core(s), from which a stronger wake formation becomes evident. These conditions contribute significantly to the flapping and recirculation region(s) found in the wake of each jet in the  $xz$  plane and in turn the presence of strong eddies and circulation magnitudes. In general, their orientation (clockwise or counter clockwise) follows that of the shear layer vortices described previous in Fig. 18, with the majority of negative and positive circulation values found on the positive and negative sides of the  $z$ -axis, respectively. These values initially appear in distinct regions at the lowest velocity ratio (Fig. 19a) and begin to overlap just downstream of the immediate jet penetration (most evident in Fig. 19c  $x/D > 2$ ) for higher velocity ratios.

The tandem jet configurations exhibit considerable differences across all velocity ratios tested, as evident in Fig. 19d, e and f. For the  $V_j/U_\infty = 0.9$  case, the largest cluster of  $N_\Omega$  is found in the region  $1 < x/D < 2$  which is markedly different than that of  $V_j/U_\infty = 1.7$  where approximately  $-1 < x/D < 0$  appears most dense. It is clear that the leading jet penetration and shielding effects entice new or additional regions

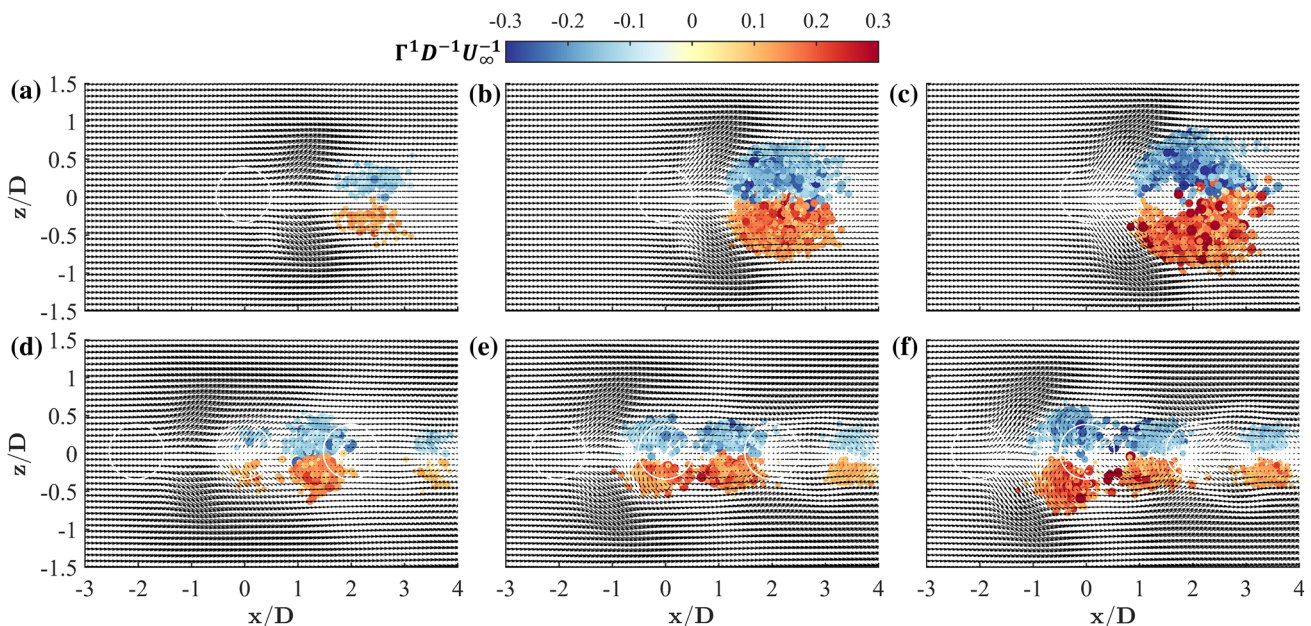


**Fig. 19** a Single and (b) tandem jet vortex center points with relative sizes and circulations,  $\Gamma^1 D^{-1} U_\infty^{-1}$ , from the POD reconstructed instantaneous velocity fields at  $V_j/U_\infty = 0.9, 1.25, 1.7$  as seen in first, second and third column, respectively

**Table 2** Statistical results of identified vortices from the TR-PIV data for velocity ratios  $V_j/U_\infty=0.9, 1.25$  and  $1.7$  for both the single and tandem jet configurations. Statistics include: total number of detected vortices,  $N_\omega$ , vortex population,  $N_\omega/A_f$ , the non-dimensionalized

|  | $V_j/U_\infty=0.9$ |        | $V_j/U_\infty=1.25$ |        | $V_j/U_\infty=1.7$ |        |
|--|--------------------|--------|---------------------|--------|--------------------|--------|
|  | Single             | Tandem | Single              | Tandem | Single             | Tandem |
| $N_\omega$ [counts]                      | 178                | 1087   | 3120                | 2428   | 3887               | 3071   |
| $N_\omega/A_f$ [counts/mm <sup>2</sup> ] | 0.04               | 0.23   | 0.66                | 0.51   | 0.82               | 0.65   |
| $\mu_A/D^2$                              | 0.496              | 0.637  | 0.556               | 0.508  | 0.554              | 0.449  |
| $\sigma_A/D^2$                           | 0.157              | 0.310  | 0.213               | 0.233  | 0.226              | 0.201  |
| $\mu_\Gamma^1 D^{-1} U_\infty^{-1}$      | 0.116              | 0.121  | 0.153               | 0.128  | 0.178              | 0.141  |
| $\sigma_\Gamma^1 D^{-1} U_\infty^{-1}$   | 0.030              | 0.047  | 0.047               | 0.044  | 0.059              | 0.048  |

mean and standard deviation of the vortex area,  $\mu_A/D^2$  and  $\sigma_A/D^2$ , respectively and the non-dimensionalized mean and standard deviation of the circulation,  $\mu_\Gamma^1 D^{-1} U_\infty^{-1}$  and  $\sigma_\Gamma^1 D^{-1} U_\infty^{-1}$ , respectively

of vortex formation, but in general inhibit the total number of identified vortices as compared to the single jet configurations at equivalent velocity ratios. There is also significantly less overlap between positive and negative circulation regions for the tandem jets as compared to the single jet, though it is unclear from the current measurement field of view if this sentiment is consistent further downstream.

Statistical results of the identified vortices are summarized quantitatively in Table 2. There is a significant difference in the number of detected vortices below and above a velocity ratio of unity for the single jet that is not reflected by the tandem jets. This provides a quantitative view of the jet's inability to overcome the crossflow and is clearly dominated by the effects of shear layer vortices without significant wake vortices. While the same is most likely true of tandem jets below unity, there are still ~6 times as many vortices identified at  $V_j/U_\infty=0.9$  for the tandem jets compared to the single jet. The vortex populations,  $N_\omega/A_f$ , where  $A_f$  is the flow area, yield contradictory findings below and above a velocity ratio of unity: for the  $V_j/U_\infty=0.9$  case the tandem array provides a substantially higher vortex population and for the  $V_j/U_\infty>1$  cases, the single jet manages to surpass the equivalent tandem jet quantities. The normalized mean and standard deviation of the vortex areas,  $\mu_A/D^2$  and  $\sigma_A/D^2$ , respectively, appear to be less dependent on the range of velocity ratios tested. Note that the  $\sigma$  values here are not to be confused with those representing the singular values in Sect. 3.2.2. Mean vortex areas reported for the single jet appear largely consistent across the range of velocity ratios tested, with only an 11.7% increase from  $0.9 \leq V_j/U_\infty \leq 1.7$ . The tandem jet vortex areas on the other hand decrease substantially, with a 41.9% decrease in size across the entire velocity ratio range. The absolute value of the circulations is considered, before calculating the normalized mean of

circulation,  $\mu_\Gamma^1 D^{-1} U_\infty^{-1}$  and standard deviation  $\sigma_\Gamma^1 D^{-1} U_\infty^{-1}$ . In general the mean circulation of the single and tandem jet configurations also exhibit opposite comparisons below and above a velocity ratio of unity. At  $V_j/U_\infty=0.9$ , the single jet has a mean circulation that is ~4% less than that reported for the tandem jets, but ~20% and ~26% higher than the tandem jets for  $V_j/U_\infty=1.25$  and  $1.7$ , respectively. When considering the standard deviation of these values, it is reasonable to say that the single jet exhibits circulation magnitudes that are nearly identical to the Table 4 tandem jet for velocity ratios below unity and notably higher for values above unity. It is clear that the vortex statistics exhibit markedly different relationships and functions with respect to velocity ratio and jet configuration. These statistics are intended to aid in future high-fidelity numerical investigations that seek to capture the flow rotation and unsteady effects found in single and tandem jets at low velocity ratios.

## 4 Conclusions

Time-resolved particle image velocimetry (TR-PIV) measurements are conducted on both a single and triple tandem jet array with  $2D$  spacing in a crossflow. Three jet to crossflow velocity ratios are examined:  $V_j/U_\infty = 0.9, 1.25, 1.7$  with an identical turbulent uniform crossflow inlet condition for each. The TR-PIV measurements are investigated in the transverse ( $xy$ ) and spanwise ( $xz$ ) planes. From the  $xy$  plane measurements, jet exit profiles are provided without the presence of a crossflow, i.e. as free jets, to ensure an equivalent mass flow rate distribution at the exit of each jet for each velocity ratio tested. The exit profiles are then investigated with the presence of the crossflow, from which it is revealed that across all velocity ratios tested,

the encapsulated middle jet exhibits the highest transverse velocities, implying that both the front and rear jets provide shielding to their common neighbor. Jet streamline trajectories, recirculation regions and penetration depths suggest that for the low velocity ratios examined, the triple jet exhibits highly localized or unique flow features, contrary to previous findings for high velocity ratio ( $V_j/U_\infty \geq 2$ ) cases. Streamline jet trajectories are collapsed for each jet and velocity ratio tested from which it is found that the conventional ' $r\delta$ ' scaling provides a better collapse of the data than ' $rD$ ' scaling, highlighting the significance of the boundary layer towards determining a universal scaling for multiple tandem jets. Collapsed recirculation zones for each jet at a given velocity ratio show both distinct areas of overlap and unique features between the tandem and single jet. Interestingly, the ratio of each tandem jet to single jet recirculation area appears to be constant for the cases where  $V_j/U_\infty > 1$ . Tandem jet penetrations increase with each additional jet downstream and appear to scale linearly with velocity ratio. For velocity ratios above unity, the variation found in jet 2 and jet 3 penetration depths are nearly identical and may exhibit similar mixing characteristics despite their differences in trajectories found from the streamline analysis. The results are reaffirmed through ensemble averaged statistics, including the ensemble averaged velocity and shear stress profiles with corresponding uncertainties. Several reference measurements are provided that seek to further constrain the experimental results for potential future numerical validation efforts.

In the  $xz$  plane, spanwise measurements at the  $y/D = 1$  location reveal periodic motions of the instantaneous velocity fields, symmetric about the  $x$ -axis. Proper orthogonal decomposition (POD) is applied to better understand the dominant coherent structures found in the near field  $xz$  plane of the jets. An optimal hard threshold procedure is incorporated to determine a suitable truncation for both the streamwise and spanwise components of velocity. It is found that the number of modes required for the tandem jets is in general a stronger function of velocity ratio than that of the single jets, as a result of the increase in kinetic energy and inherent noise in the velocity fields. The eigenvector shapes reveal the presence of additional secondary instabilities in the tandem jet flow, particularly in the spanwise velocity

component, that are not present in the single jet at equivalent velocity ratio. The presence of these secondary structures is largely a function of the induced turbulence of each jet ( $Re \sim 10^4$ ) and the crossflow ( $Re \sim 10^5$ ) and the associated shielding effects. It remains to be seen if the jets exhibit more coherent shapes at lower Reynolds numbers and if the jets do indeed exhaust into the crossflow in a more coherent manner, how these conditions would affect the shielding of each tandem jet. The velocity fields are then reconstructed and vorticity contours show the transition process in vortex development in the  $xz$  plane. From the ensemble-averaged vorticity contours, it is found that contrary to the classical single jet, which typically exhibits a circular region of little to no vorticity in the core of the jet, the tandem jets exhibit crescent moon-shaped gaps in the interstitial regions between each wake formation. Vortex identification algorithms complete the investigation of the wake profiles and provide valuable insight into the centers, sizes and circulation magnitudes of the identified vortices. These results provide several useful statistics across the spectrum of velocity ratios tested, citing major differences below and above velocity ratios of unity, as the jets' momentum overcomes that of the crossflow, thereby producing larger wake formations and swirling. Investigation of the spanwise plane of the single and tandem jets in crossflow further supply high fidelity numerical modeling efforts that seek to replicate the wakes of tandem jet arrays at low velocity ratios.

This study provides experimental evidence of several transition processes that occur for multiple tandem jets in a crossflow at low velocity ratios, with a single jet at analogous testing conditions for comparison. Ongoing work based on the existing data sets will seek to identify the vortical formations of these instantaneous profiles more directly towards universal scaling of the tandem jet trajectories. The data provides statistical flow characterization, reference parameters, inlet and boundary conditions and uncertainties to aid analogous computational efforts.

## Appendix: Test cases

See Tables 3 and 4



**Table 3** Experimental test conditions for the single jet in crossflow. For each element, three numbers imply conditions for velocity ratios  $V_j/U_\infty = 0.92, 1.26$  and  $1.70$ . If only one number is present in a given element, it is consistent across all three velocity ratios tested

| Metric                                    | Units   | Nominal Value | Total, $\mu_i$ | Systematic, $b_i$ | Random, $s_i$ |
|---|---|---------------|----------------|-------------------|---------------|
| <b>Velocity (T.K.E.)</b>                  |   |               |                |                   |               |
| Crossflow, $U_\infty$ ( $k_\infty$ )      | $\text{m}^1\text{s}^{-1}$ ( $\text{m}^2\text{s}^{-2}$ ) | 9.52 (0.57)   | 0.78 (0.0)     | 0.78 (0.0)        | 0.0 (0.0)     |
| Jet, $V_j$ ( $k_j$ )                      | $\text{m}^1\text{s}^{-1}$ ( $\text{m}^2\text{s}^{-2}$ ) | 8.74 (5.37)   | 0.13 (0.0)     | 0.13 (0.0)        | 0.0 (0.0)     |
|   |   | 12.04 (13.23) | 0.13 (0.0)     | 0.13 (0.0)        | 0.0 (0.0)     |
|   |   | 16.20 (20.57) | 0.13 (0.0)     | 0.13 (0.0)        | 0.0 (0.0)     |
| <b>Temperatures</b>                       |   |               |                |                   |               |
| Crossflow, $T_\infty$                     | K   | 297.3         | 0.85           | 0.85              | 0.0           |
|   |   | 297.32        | 0.85           | 0.85              | 0.0           |
|   |   | 297.41        | 0.85           | 0.85              | 0.0           |
| Jet, $T_j$                                | K   | 305.36        | 0.84           | 0.84              | 0.0           |
|   |   | 307.10        | 0.84           | 0.84              | 0.0           |
|   |   | 309.28        | 0.84           | 0.84              | 0.0           |
| Ambient, $T_{amb}$                        | K   | 297.17        | 0.86           | 0.85              | 0.16          |
| <b>Fluid Properties</b>                   |   |               |                |                   |               |
| Crossflow Density, $\rho_\infty$          | $\text{kg}^1\text{m}^{-3}$                              | 1.187         | 0.004          | 0.004             | 0.0           |
|   |   | 1.187         | 0.004          | 0.004             | 0.0           |
|   |   | 1.186         | 0.004          | 0.004             | 0.0           |
| Jet Density, $\rho_j$                     | $\text{kg}^1\text{m}^{-3}$                              | 1.155         | 0.004          | 0.004             | 0.0           |
|   |   | 1.149         | 0.004          | 0.004             | 0.0           |
|   |   | 1.141         | 0.004          | 0.004             | 0.0           |
| Crossflow Dynamic Viscosity, $\mu_\infty$ | $\text{kg}^1\text{m}^{-1}\text{s}^{-1}$                 | 1.84E-05      | 1.47E-07       | 1.47E-07          | 0.0           |
|   |   | 1.84E-05      | 1.47E-07       | 1.47E-07          | 0.0           |
|   |   | 1.84E-05      | 1.47E-07       | 1.47E-07          | 0.0           |
| Jet Dynamic Viscosity, $\mu_j$            | $\text{kg}^1\text{m}^{-1}\text{s}^{-1}$                 | 1.87E-05      | 1.50E-07       | 1.50E-07          | 0.0           |
|   |   | 1.88E-05      | 1.51E-07       | 1.51E-07          | 0.0           |
|   |   | 1.89E-05      | 1.51E-07       | 1.51E-07          | 0.0           |
| Pressure Gage, $\Delta P$                 | Pa  | -46.89        | 4.42           | 4.42              | 0.0           |
|   |   | -47.70        | 4.50           | 4.50              | 0.0           |
|   |   | -48.11        | 4.54           | 4.54              | 0.0           |
| Ambient Pressure, $P_{amb}$               | kPa   | 101.28        | 5.36           | 5.36              | 0.07          |
| Relative Humidity, $\phi$                 | %   | 53.4          | 2.9            | 2.7               | 1.2           |
| <b>Non-Dimensional</b>                    |   |               |                |                   |               |
| Boundary Layer, $\delta_j/D$              |   | 0.46          |                |                   |               |
| Reynolds Number, $Re_\infty$              |   | 1.82E+05      | -              |                   |               |
| Reynolds Number, $Re_j$                   |   | 1.20E+04      | -              |                   |               |
|   |   | 1.63E+04      |                |                   |               |
|   |   | 2.17E+04      |                |                   |               |
| $V_j/U_\infty$                            |   | 0.92          | -              |                   |               |
|   |   | 1.26          |                |                   |               |
|   |   | 1.70          |                |                   |               |

**Table 4** Experimental test conditions for the tandem jets in crossflow. The element values follow the same convention as Table 3

| Metric  | Units                       | Nominal Value    | Total, $\mu_i$ | Systematic, $b_i$ | Random, $s_i$ |
|---|-----------------------------|------------------|----------------|-------------------|---------------|
| <b>Velocity (T.K.E.)</b>  |                             |                  |                |                   |               |
| Crossflow, $U_\infty$ ( $k_\infty$ )                                    | $m^1s^{-1}$ ( $m^2s^{-2}$ ) | 9.52 (0.57)      | 0.78 (0.0)     | 0.78 (0.0)        |               |
| Jet 1, $V_{j1}$ ( $k_{j1}$ )  | $m^1s^{-1}$ ( $m^2s^{-2}$ ) | 8.42 (4.20)      | 0.82 (0.0)     | 0.82 (0.0)        |               |
|   |                             | 12.11 (5.85)     | 0.82 (0.0)     | 0.82 (0.0)        |               |
|   |                             | 15.91 (7.74)     | 0.82 (0.0)     | 0.82 (0.0)        |               |
| Jet 2, $V_{j2}$ ( $k_{j2}$ )  | $m^1s^{-1}$ ( $m^2s^{-2}$ ) | 8.81 (1.96)      | 1.82 (0.0)     | 1.82 (0.0)        |               |
|   |                             | 12.22 (3.03)     | 1.82 (0.0)     | 1.82 (0.0)        |               |
|   |                             | 15.63 (4.46)     | 1.82 (0.0)     | 1.82 (0.0)        |               |
| Jet 3, $V_{j3}$ ( $k_{j3}$ )  | $m^1s^{-1}$ ( $m^2s^{-2}$ ) | 8.50 (1.87)      | 0.87 (0.0)     | 0.87 (0.0)        |               |
|   |                             | 12.06 (2.10)     | 0.87 (0.0)     | 0.87 (0.0)        |               |
|   |                             | 15.74 (3.21)     | 0.87 (0.0)     | 0.87 (0.0)        |               |
| <b>Temperatures</b>   |                             |                  |                |                   |               |
| Crossflow, $T_\infty$   | K                           | 296.54           | 0.89           | 0.85              | 0.28          |
|   |                             | 296.73           | 0.89           | 0.85              | 0.27          |
|   |                             | 296.87           | 0.92           | 0.85              | 0.35          |
| Jet 1, $T_{j1}$   | K                           | 296.6            | 0.87           | 0.87              | 0.10          |
|   |                             | 297.62           | 0.88           | 0.87              | 0.13          |
|   |                             | 299.55           | 0.98           | 0.87              | 0.45          |
| Jet 2, $T_{j2}$   | K                           | 296.54           | 0.85           | 0.84              | 0.10          |
|   |                             | 297.76           | 0.86           | 0.84              | 0.16          |
|   |                             | 300.02           | 1.00           | 0.84              | 0.54          |
| Jet 3, $T_{j3}$   | K                           | 296.5            | 0.85           | 0.85              | 0.09          |
|   |                             | 297.55           | 0.86           | 0.85              | 0.17          |
|   |                             | 299.55           | 1.01           | 0.85              | 0.56          |
| Ambient, $T_{amb}$  | K                           | 296.5            | 0.85           | 0.85              | 0.11          |
|   |                             | 296.5            | 0.85           | 0.85              | 0.11          |
|   |                             | 296.5            | 0.85           | 0.85              | 0.11          |
| <b>Fluid Properties</b>   |                             |                  |                |                   |               |
| Crossflow   | $kg^1 m^{-3}$               | 1.187            | 0.004          | 0.004             | 0.0           |
| Density, $\rho_\infty$  |                             | 1.187            | 0.004          | 0.004             | 0.0           |
|   |                             | 1.186            | 0.004          | 0.004             | 0.0           |
| Aggregate Jet   | $kg^1 m^{-3}$               | 1.187            | 0.0            | 0.0               | 0.0           |
| Density, $\rho_j$   |                             | 1.185            | 0.0            | 0.0               | 0.0           |
|   |                             | 1.185            | 0.0            | 0.0               | 0.0           |
| Crossflow   | $kg^1 m^{-3}$               | 1.83E-05         | 1.46E-07       | 1.46E-07          | 0.0           |
| Dynamic Viscosity, $\mu_\infty$   |                             | 1.83E-05         | 1.46E-07       | 1.46E-07          | 0.0           |
|   |                             | 1.83E-05         | 1.46E-07       | 1.46E-07          | 0.0           |
| Aggregate   | $kg^1 m^{-3}$               | 1.83E-05         | 0.0            | 0.0               | 0.0           |
| Jet Dynamic   |                             | 1.83E-05         | 0.0            | 0.0               | 0.0           |
| Viscosity, $\mu_j$  |                             | 1.83E-05         | 0.0            | 0.0               | 0.0           |
| Pressure Gage, $\Delta P$   | Pa                          | -56.58           | 5.58           | 5.34              | 1.63          |
|   |                             | -55.39           | 5.48           | 5.23              | 1.66          |
|   |                             | -56.23           | 5.56           | 5.30              | 1.67          |
| Ambient Pressure, $P_{amb}$   | kPa                         | 101.14           | 5.35           | 5.35              | 0.11          |
| Relative Humidity, $\phi_{amb}$   |                             | 54.9             | 2.9            | 2.7               | 1.1           |
| <b>Non-Dimensional</b>  |                             |                  |                |                   |               |
| Boundary Layer Thickness, $\delta_{j1}/D, \delta_{j2}/D, \delta_{j3}/D$ |                             | 0.40, 0.46, 0.53 |                |                   |               |
| Reynolds Number, $Re_\infty$  |                             | 1.82E+05         |                |                   |               |
|   |                             | 1.82E+05         |                |                   |               |
|   |                             | 1.82E+05         |                |                   |               |
| Reynolds Number, $Re_j$   |                             | 1.24E+04         |                |                   |               |
|   |                             | 1.74E+04         |                |                   |               |
|   |                             | 2.26E+04         |                |                   |               |
| $V_j/U_\infty$  |                             | 0.90             |                |                   |               |
|   |                             | 1.27             |                |                   |               |
|   |                             | 1.66             |                |                   |               |

**Acknowledgements** The authors gratefully acknowledge support from Nuclear Energy University Program (NEUP) through the following projects: NEUP 12-3582 entitled “Experimentally Validated Numerical Models of Non-Isothermal Turbulent Mixing in High Temperature Reactors”. NEUP 15-8627 “Experimental Validation Data and Computational Models for Turbulent Mixing of Bypass and Coolant Jet Flows in Gas-Cooled Reactors”.

## References

- Amini N, Hassan YA (2009) Measurements of jet flows impinging into a channel containing a rod bundle using dynamic PIV. *Int J Heat Mass Transf* 52:5479–5495. <https://doi.org/10.1016/j.ijheatmasstransfer.2009.07.002>
- Anazadehsayed A, Barzegar Gerdroodbary M, Amini Y, Moradi R (2017) Mixing augmentation of transverse hydrogen jet by injection of micro air jets in supersonic crossflow. *Acta Astronaut* 137:403–414. <https://doi.org/10.1016/j.actaastro.2017.05.007>
- Andreopoulos J, Rodi W (1984) Experimental investigation of jets in a crossflow. *J Fluid Mech* 138:93–127
- Bernero S, Fiedler HE (2000) Application of particle image velocimetry and proper orthogonal decomposition to the study of a jet in a counterflow. *Exp Fluids* 29:S274–S281
- Bonnet JP (1994) Stochastic estimation and proper orthogonal decomposition: complementary techniques for identifying structure. *Exp Fluids* 17:307–314
- Bons JP, Sondergaard R, Rivir RB (2002) The Fluid Dynamics of LPT Blade Separation Control Using Pulsed Jets. *J Turbomach* 124:77–85. <https://doi.org/10.1115/1.1425392>
- Brunton SL, Kutz JN (2019) Data-driven science and engineering: Machine learning, dynamical systems and control. Cambridge University Press
- Cambonie T, Aider J-L (2014) Transition scenario of the round jet in crossflow topology at low velocity ratios. *Phys Fluids*. <https://doi.org/10.1063/1.4891850>
- Cambonie T, Gautier N, Aider JL (2013) Experimental study of counter-rotating vortex pair trajectories induced by a round jet in crossflow at low velocity ratios. *Exp Fluids*. <https://doi.org/10.1007/s00348-013-1475-9>
- Crafton J, Forlines A, Palluconi S, Hsu K-Y, Carter C, Gruber M (2015) Investigation of transverse jet injections in a supersonic crossflow using fast-responding pressure-sensitive paint. *Exp Fluids*. <https://doi.org/10.1007/s00348-014-1877-3>
- Figliola RS, Beasley DE (2011) Theory and Design for Mechanical Measurements. John Wiley and Sons, Inc.
- Florschuetz LW, Su CC (1987) Effects of crossflow temperature on heat transfer within an array of impinging jets. *J Heat Transfer* 109:74–82
- Florschuetz LW, Truman CR, Metzger DE (1981) Streamwise flow and heat transfer distributions for jet array impingement with cross flow. *J Heat Transfer* 103:337–342
- Gardner JE, Burgisser A, Stelling P (2007) Eruption and deposition of the Fisher Tuff (Alaska): evidence for the evolution of pyroclastic flows. *J Geol* 115:417–435
- Gavish M, Donoho DL (2014) The Optimal Hard Threshold for Singular Values is 4/3. *IEEE Trans Inf Theory* 60:5040–5053. <https://doi.org/10.1109/tit.2014.2323359>
- Gopalan S, Abraham BM, Katz J (2004) The structure of a jet in cross flow at low velocity ratios. *Phys Fluids* 16:2067–2087. <https://doi.org/10.1063/1.1697397>
- Graftieaux L, Michard M, Grosjean N (2001) Combining PIV, POD and vortex identification algorithms for the study of unsteady turbulent swirling flows. *Meas Sci Technol* 12:1422–1429
- Günther T, Theisel H (2018) The State of the Art in Vortex Extraction. *Computer Graphics Forum* 37:149–173. <https://doi.org/10.1111/cgf.13319>
- Gutmark EJ, Ibrahim IM, Murugappan S (2011) Dynamics of single and twin circular jets in cross flow. *Exp Fluids* 50:653–663. <https://doi.org/10.1007/s00348-010-0965-2>
- Holmes P, Lumley JL, Berkooz G (1996) Turbulence, Coherent Structures, Dynamical Systems and Symmetry. Cambridge University Press
- Huang Y, Ekkad SV, Han J-C (1998) Detailed Heat Transfer Distributions Under an Array of Orthogonal Impinging Jets. *J Thermophys Heat Transfer* 12:73–79. <https://doi.org/10.2514/2.6304>
- Isaac KM, Jakubowski AK (1985) Experimental study of the interaction of multiple jets with a cross flow. *AIAA Journal* 23:1679–1683. <https://doi.org/10.2514/3.9151>
- Kaffel A, Moureh J, Harion J-L, Russeil S (2016) TR-PIV measurements and POD analysis of the plane wall jet subjected to lateral perturbation. *Exp Thermal Fluid Sci* 77:71–90. <https://doi.org/10.1016/j.expthermflusci.2016.04.001>
- Karagozian AR (2010) Transverse jets and their control. *Prog Energy Combust Sci* 36:531–553. <https://doi.org/10.1016/j.pecs.2010.01.001>
- Kelso RM, Lim TT, Perry AE (1996) An experimental study of round jets in a cross-flow. *J Fluid Mech* 306:111–144
- Kolář V, Savory E (2007) Dominant flow features of twin jets and plumes in crossflow. *J Wind Eng Ind Aerodyn* 95:1199–1215. <https://doi.org/10.1016/j.jweia.2007.02.025>
- Kolář V, Takao H, Todoroki T, Savory E, Okamoto S, Toy N (2003) Vorticity transport within twin jets in crossflow. *Exp Thermal Fluid Sci* 27:563–571. [https://doi.org/10.1016/s0894-1777\(02\)00270-4](https://doi.org/10.1016/s0894-1777(02)00270-4)
- Kristo PJ, Sohail S, Reed RS, Kimber ML (2020) Low speed wind tunnel flow diagnostics and benchmark cases for thermal fluids CFD validation efforts. *engrXiv*. <https://doi.org/10.31224/osf.io/k26rp>
- Krothapalli A, Lourenco L, Buchlin JM (1990) Separated flow upstream of a jet in a crossflow. *AIAA Journal* 28:414–420. <https://doi.org/10.2514/3.10408>
- Kutz JN, Brunton SL, Brunton BW, Proctor JL (2016) Dynamic mode decomposition: data-driven modeling of complex systems. Society for Industrial and Applied Mathematics
- Landfried DT, Kristo PJ, Clifford CE, Kimber ML (2019) Design of an experimental facility with a unit cell test section for studies of the lower plenum in prismatic high temperature gas reactors. *Ann Nucl Energy* 133:236–247. <https://doi.org/10.1016/j.anucene.2019.05.037>
- Li Z, Huai W, Qian Z (2012) Study on the flow field and concentration characteristics of the multiple tandem jets in crossflow. *Science China Technological Sciences* 55:2778–2788. <https://doi.org/10.1007/s11431-012-4964-9>
- Ling J, Ruiz A, Lacaze G, Oefelein J (2016) Uncertainty Analysis and Data-Driven Model Advances for a Jet-in-Crossflow. *J Turbomach*. <https://doi.org/10.1115/1.4034556>
- Lohse J, Barth HP, Nitsche W (2016) Active control of crossflow-induced transition by means of in-line pneumatic actuator orifices. *Exp Fluids*. <https://doi.org/10.1007/s00348-016-2213-x>
- Lumley JL (1967) The structure of inhomogeneous turbulent flows. Atmospheric turbulence and radio wave propagation. 23:166–178
- M’Closkey RT, King JM, Cortelezzi L, Karagozian AR (2002) The actively controlled jet in crossflow. *J Fluid Mech* 452:325–335. <https://doi.org/10.1017/s0022112001006589>
- Mahesh K (2013) The Interaction of Jets with Crossflow. *Annu Rev Fluid Mech* 45:379–407. <https://doi.org/10.1146/annurev-fluid-120710-101115>
- Margason RJ (1993) Fifty years of jet in cross flow research AGARD-CP5341. 56; 1–141
- Meyer KE, Pedersen JM, Özcan O (2007) A turbulent jet in crossflow analysed with proper orthogonal decomposition. *J Fluid Mech* 583:199–227. <https://doi.org/10.1017/s0022112007006143>



- Muppidi S, Mahesh K (2005) Study of trajectories of jets in crossflow using direct numerical simulations. *J Fluid Mech* 530:81–100. <https://doi.org/10.1017/s0022112005003514>
- Narayanan S, Barooah P, Cohen JM (2003) Dynamics and Control of an Isolated Jet in Crossflow. *AIAA Journal* 41:2316–2330. <https://doi.org/10.2514/2.6847>
- New TH, Lim TT, Luo SC (2006) Effects of jet velocity profiles on a round jet in cross-flow. *Exp Fluids* 40:859–875. <https://doi.org/10.1007/s00348-006-0124-y>
- New TH, Zang B (2015) On the trajectory scaling of tandem twin jets in cross-flow in close proximity. *Exp Fluids*. <https://doi.org/10.1007/s00348-015-2070-z>
- Nguyen T, Muyschondt R, Hassan YA, Anand NK (2019a) Experimental investigation of cross flow mixing in a randomly packed bed and streamwise vortex characteristics using particle image velocimetry and proper orthogonal decomposition analysis. *Phys Fluids*. <https://doi.org/10.1063/1.5079303>
- Nguyen T, White L, Vaghetto R, Hassan Y (2019b) Turbulent flow and vortex characteristics in a blocked subchannel of a helically wrapped rod bundle. *Exp Fluids*. <https://doi.org/10.1007/s00348-019-2778-2>
- Pratte BD, Baines WD (1967) Profiles of the round turbulent jet in a cross flow. *Journal of the Hydraulics Division* 93:53–64
- Pritchard PJ (2011) Fox and McDonald's Introduction to Fluid Mechanics. John Wiley and Sons, Inc
- Reed RS, Weiss AW, Kristo PJ, Kimber ML (2020) Hydraulic Comparison of Single and Multiple-Jet Impingement on a Flate Plate 5th Thermal and Fluids Engineering Conference (TFEC). ASTFE Digital Library, Virtual
- Ruiz AM, Lacaze G, Oefelein JC (2015) Flow topologies and turbulence scales in a jet-in-cross-flow. *Phys Fluids*. <https://doi.org/10.1063/1.4915065>
- Sciacchitano A, Neal DR, Smith BL et al (2015) Collaborative framework for PIV uncertainty quantification: comparative assessment of methods. *Meas Sci Technol* 26:074004. <https://doi.org/10.1088/0957-0233/26/7/074004>
- Sciacchitano A, Wieneke B (2016) PIV uncertainty propagation. *Meas Sci Technol* 27:084006. <https://doi.org/10.1088/0957-0233/27/8/084006>
- Shapiro SR, King JM, M'Closkey RT, Karagozian AR (2006) Optimization of Controlled Jets in Crossflow. *AIAA Journal* 44:1292–1298. <https://doi.org/10.2514/1.19457>
- Sirovich L (1987) Turbulence and the dynamics of coherent structures. I. Coherent structures Quarterly of Applied Mathematics 45:561–571
- Smith BL, Neal DR, Feero MA, Richards G (2018) Assessing the limitations of effective number of samples for finding the uncertainty of the mean of correlated data. *Meas Sci Technol*. <https://doi.org/10.1088/1361-6501/aae91d>
- Smith SH, Mungal MG (1998) Mixing, structure and scaling of the jet in crossflow. *J Fluid Mech* 357:83–122
- Taira K, Brunton SL, Dawson STM et al (2017) Modal Analysis of Fluid Flows: An Overview. *AIAA Journal* 55:4013–4041. <https://doi.org/10.2514/1.J056060>
- Vernet R, Thomas L, David L (2009) Analysis and reconstruction of a pulsed jet in crossflow by multi-plane snapshot POD. *Exp Fluids* 47:707–720. <https://doi.org/10.1007/s00348-009-0730-6>
- Wieneke B (2015) PIV uncertainty quantification from correlation statistics. *Meas Sci Technol* 26:074002. <https://doi.org/10.1088/0957-0233/26/7/074002>
- Yu D, Ali MS, Lee JHW (2006) Multiple Tandem Jets in Cross-Flow. *Journal of Hydraulic Engineering* 132:971–982
- Yuan LL, Street RL (1998) Trajectory and entrainment of a round jet in crossflow. *Phys Fluids* 10:2323–2335. <https://doi.org/10.1063/1.869751>
- Ziegler H, Woller PT (1973) Analysis of Stratified and Closely Spaced Jets Exhausting into a Crossflow.

**Publisher's Note** Springer Nature remains neutral with regard to jurisdictional claims in published maps and institutional affiliations.